A comparison of radon, heat tracer and head gradient methods to quantify surface water - groundwater exchange in a tidal wetland (Kooragang Island, Newcastle, Australia)

Mahmood Sadat-Noori*, Christian Anibas, Martin S. Andersen, William Glamore

Water Research Laboratory, School of Civil & Environmental Engineering, UNSW Sydney, NSW 2052, Australia

*Corresponding author:

M. Sadat-Noori, Water Research Laboratory, School of Civil & Environmental Engineering, University of New South Wales,110 King St., Manly Vale, NSW, 2093, Australia

Email: m.sadat-noori@unsw.edu.au

Tel: (+61) 2 8071 9879

Abstract

Subsurface flow plays an important role in the functioning of wetlands and in the maintenance of their ecosystem services. Specifically, the transport and exchange of dissolved matter between sediments and surface waters is regulated by subsurface flow, which can strongly affect ecological zonation and productivity. Having a quantitative understanding of this subsurface flow is therefore important. Field techniques based on Darcy's equation or natural tracers are often used separately to assess flows. Here, radon and heat (both natural groundwater tracers) and Darcy's equation are used simultaneously to quantify the subsurface flow in a tidal wetland (Kooragang Island, Newcastle, Australia) and the results of the independent methods are compared. A steady-state radon mass balance model indicated an overall net subsurface exfiltration of 10.2 ± 4.2 cm/d while a 1D, vertical fluid heat transport model indicated a net exfiltration of 4.3 ± 2.9 cm/d. Flow estimated from analysis of hydraulic heads indicated an exfiltration rate of 3.2 ± 1.8 cm/d. The difference in flow rates is likely due to the localised measurement of the heat and head methods relative to radon, and therefore, these methods are less likely to capture zones of preferential subsurface flow. The main advantage of radon is that it provides the total subsurface flow regardless of the driving force. While head gradient or heat tracer method have the advantage of temporally quantify infiltration and exfiltration, we highlight that these methods may underestimate subsurface flows in highly dynamic coastal systems, such as tidal wetlands where a large portion of the subsurface flow is recirculated seawater. This could potentially lead to errors in solute flux estimates. This study highlights the importance of employing a multi-tracer approach and has implications towards quantifying the hydrological export of dissolved constituents (e.g., carbon and nitrogen) in coastal wetlands.

Keywords: Coastal wetland, wetland hydrology, natural groundwater tracer, temperature, groundwater-surface water interaction.

1 Introduction

Coastal wetlands are highly productive ecosystems that provide valuable ecosystem services (e.g. nutrient cycling, water quality, fisheries and recreation) (McLaughlin and Cohen, 2013). Hydrologic dynamics play a critical role in the functioning of tidal wetlands as tides are a strong driver of change (Guo et al., 2009; Johnston et al., 2011). For example carbon sequestration, sedimentological processes, natural coastal protection, and water quality depend on the hydrology of coastal wetlands (Bullock and Acreman, 2003; Muneepeerakul et al., 2008). Subsurface flow and/or porewater exchange plays an important role in coastal wetland hydrology and provides a pathway for solute transport at the sediment-water interface (Kwon et al., 2014; Sadat-Noori and Glamore, 2019; Webb et al., 2019). Identifying and quantifying the subsurface flow in wetlands can provide an improved understanding on how groundwater contributes to surface water quantity, quality and the functioning of ecosystems in coastal wetland environments (Conant et al., 2019; Knights et al., 2017; Montiel et al., 2018). However, subsurface flows are particularly complex processes due to their spatial and temporal heterogeneity, and hence, are often the least quantified component of a wetland hydrology water balance (Webb et al., 2017).

Subsurface flow can occur regardless of the water composition (fresh or saline), with the driving forces being groundwater hydraulic gradients, surface water runoff events, and tidal pumping (Santos et al., 2012). Water exchange may also be driven by gradients in salinity and when unstable density distributions are created by saltwater overlying freshwater (Santos et al., 2012). Different methods have been used to investigate water exchange at the sediment-water interface, including seepage meters (Rosenberry et al., 2020), artificial tracers (Cook et al., 2018a), and traditional hydrometric methods analysing head data (Qu et al., 2017). To overcome the challenges of quantifying subsurface flow using hydrometric methods, natural tracers have also been widely applied (Cook et al., 2018b). Radon (^{222}Rn) and heat are two of the most effective and established tracer techniques in hydro-geological research (Kurylyk et al., 2018; Rau et al., 2014; Ren et al., 2018). Many studies have used these techniques to quantify groundwater movement (Li et al., 2019), study groundwater-surface water interactions, (Anibas et al., 2011; McCallum et al., 2014; Sadat-Noori et al., 2016b) and/or estimate subsurface physical properties (Vandersteen et al., 2015). Several studies in freshwater environments have shown that multiple technique/tracer approaches provide more robust and reliable results, as different tracers are based on different physical principles, detect different aspects of groundwater flow and have different advantages (Unland et al., 2013).

Radon-222 is a noble gas with very low chemical reactivity that is usually enriched in groundwater relative to surface water (Peterson et al., 2019). Radon is produced in sediments via the decay of the radium-226 isotope. Radon decays with a half-life of 3.8 days, and this relative short half-life and volatility means that it does not travel far in surface waters from its location of discharge, hence, its presence indicates local subsurface water discharge (Burnett, 2008). Heat tracing uses temperature variations at different depth in the subsurface to model the quantity and temporal/spatial changes of the vertical component of groundwater movement by applying analytical and/or numerical solutions of combined heat conduction and advective transport. Previous research using the heat tracing technique has focused mainly on the hyporheic zones of rivers and wetlands (Anibas et al., 2012; Bravo et al., 2002; Rau et al., 2010) or tested the limits of applicability in temporal and spatial dimensions (Rau et al., 2015; Roshan et al., 2012; Sebok and Müller, 2019). In a coastal wetland, groundwater-surface water exchange is highly variable with changing flow directions during each tidal cycle (del Pilar Alvarez et al., 2015). This dynamic behavior of groundwater-surface water interaction adds to the complexity of hydrologic and thermal processes found in non-tidal wetlands and may be the reason why heat tracing is rarely used in coastal wetlands (Befus et al., 2013). Additionally, often tidal wetlands are inaccessible and the deployment of a network of measurement devices is challenging. To date, studies using the heat tracer in coastal (Kurylyk et al., 2019; Swain and Prinos, 2018) or tidal settings (Halloran et al., 2017) are limited.

Radon and heat tracers can be used independently to investigate groundwater-surface water interactions (Navarro-Martinez et al., 2017). However, researchers advise that multiple lines of evidence, by combining different techniques, can validate results and overcome limitations of a single method (Dujardin et al., 2014; Gilfedder et al., 2015). The traditional technique to investigate subsurface flow is by hydraulic gradients, which may underestimate subsurface flow compared to other techniques (Mulligan and Charette, 2006; Su et al., 2016). Studies combining radon and heat tracers are limited to inland waterbodies and focus on river water infiltrating aquifers and residence time calculations of hyporheic groundwater (Cranswick et al., 2014; Hoehn and Cirpka, 2006; Vogt et al., 2010). Heat tracing in the sediment allows for the calculation of subsurface flow at shorter temporal resolution than radon and can distinguish between infiltration and exfiltration. Heat tracing, however, provides point data and spatial extrapolation is associated with large uncertainty. Radon on the other hand, does not have this problem with spatial uncertainty, as it smooths out spatial heterogeneity and provides the total subsurface flow integrated over a certain time period. Calculating an estimate of the temporal

resolution that is less than the tidal frequency via the radon technique is only possible using a detailed numerical model. Our study builds on the only available heat study in a tidal setting (tidal creek) in the literature (Halloran et al., 2017), and aims to extend subsurface flow quantification in coastal wetlands that are dominated by tidal inundation. To achieve this aim, the study utilises time series measurements of both radon and heat tracers as well as hydraulic heads.

In groundwater discharge zones the flow directions are complex and varying in relation to the measurement location in the subsurface, but also varying over time with wave action and tidal stage (Rakhimbekova et al., 2018; Turner et al., 2016). Flow directions are further complicated by density effects when both fresh and saline water are discharging (Andersen et al., 2007). Within the discharge zone, vertical flows may dominate (but varying in direction with the tidal stage) while further inland flows are predominantly horizontal. This dependence of location needs to be taken into consideration when designing field studies. The radon tracer technique has the advantage of providing information on the total subsurface flow, regardless of its salinity or subsurface source (Burnett et al., 2007). For example, when used in tidal environments, radon integrates the discharge of both fresh regional and saline water originating from the surface but circulated through the subsurface (Su et al., 2014). For both heat tracing and Darcy methods the location and geometry of the observations (field deployment) needs to be considered. For heat tracing studies temperature sensors are traditionally deployed vertically in the sediment for practical reasons and therefore mostly deployed directly in the discharge zone. For such deployments the heat tracer technique will provide only the vertical component of flow, regardless of whether the water is fresh or saline (Rau et al., 2014). Depending on the relative location of piezometer screens, the Darcy method can be used to determine either vertical or horizontal hydraulic head gradients. In the discharge zone, vertical gradients can be determined by two or more piezometers with screened intervals vertically arranged. Further landward, laterally spaced piezometers can determine the horizontal fresh groundwater hydraulic head gradients. The gradients can be converted to flows provided the hydraulic conductivity distribution between the screens is known. Appropriately quantifying the hydraulic conductivity distribution is one of the main challenges and source of uncertainty with the Darcy method. When the methods described above are used alone, different quantitative results may be achieved representing either an integrated value (radon) or the particular parts of the system being observed (heat and Darcy), however when the different methods are used

in combination, they can provide a more comprehensive understanding of the system and therefore add more confidence in the findings when results are in agreement.

The objective of this study is to evaluate groundwater-surface water interactions in a tidal wetland using three independent methods simultaneously to 1) compare the methods of quantifying subsurface flow against each other, 2) assess the capability of the heat tracer method in quantifying subsurface flow in tidal settings, and 3) quantify various sources of the total subsurface flow by disaggregating the subsurface processes through jointly interpreting the techniques used at the study site.

2 Material and Method

2.1 Site description

The field site is a tidal wetland on Kooragang Island (-32.866707S, 151.715561E; Figure 1) in the Hunter River Estuary located near Newcastle, New South Wales, Australia. Approximately 7 km upstream of the river mouth, the wetland is a low-lying flat area with an elevation between 1.5 - 2 m above mean sea level. The field site experiences a temperate climate with an average annual rainfall of 1122 mm and an average temperature of 22.5 °C in summer and 12 °C in winter (Bureau of Meteorology; www.bom.gov.au). The wetland is connected to the Hunter River Estuary via a 170 m long and 10 m wide tidal estuarine channel. Intertidal mudflats cover an area of 113,330 m^2 of the overall catchment area (240,000 m^2). The wetland has no upstream surface water inputs; its hydrology is dominated by a semi-diurnal tidal regime with spring and neap tides. The wetland sediment is composed primarily of silt with numerous crab burrows across the intertidal zone that can increase permeability and facilitate porewater circulation (Stieglitz et al., 2013). The top 0.3 m of the sediment has a muddy texture with partly decayed organic matter, while the remaining sediment profile is dominated by estuarine silt and sand (until 5 meters below the surface). The area did not receive any rainfall in the 15 days prior to the fieldwork, however, on 29th November 2018 during the field sampling, there was a 20 mm rainfall event. The site was selected for its small catchment area and narrow estuarine mouth, which helps constrain the area under investigation. Additionally, the site was secure from the public interfering with installations yet accessible for deploying measurement instrumentation.

The Eastern and southern parts of Kooragang Island are characterized by a combination of port facilities and industrial land use, but the majority of the island, to the North and West, is part

of the Kooragang Nature Reserve. The island consists of unconsolidated quaternary sediments (Figure 2) and its hydrogeology is comprised of two sand aquifers, a shallow unconfined and a deeper confined aquifer. The shallow aquifer extends to a depth of 5 meters. The two aquifers are separated by a clay aquitard layer, which has a thickness of 4 m (Robinson, 2006). The unconfined aquifer, of primary interest to this study, is primarily recharged by rainfall directly within the Nature Reserve and the general groundwater flow on the island in the unconfined aquifer is towards the South Channel of the Hunter River Estuary (Jones, 2013). On the island, the water table in this aquifer has been identified at depths of 0.3 to 1.5 m from the surface.

2.2 Surface water measurements

Fieldwork was carried out from 26th November – 2nd December 2018 to install equipment and collect surface and groundwater data including radon, hydraulic heads, temperature time series and water quality measurements. Surface water physico-chemical parameters were measured using a calibrated multiparameter water quality sonde (Yellow Springs Instrumentation - YSI EXO_2). Variables including salinity, water temperature (±0.01 °C) and depth (±0.004 m) were collected at 15-min intervals. Wind speed data (±10%) was collected onsite using a weather station (Model PH1000). Current velocity, direction and water depth were measured in the center of the tidal channel using a Sontek Argonaut acoustic doppler current profiler (ADCP) (SonTek/YSI) at 10-min intervals. The channel cross-section depth was measured every 2 meters at high tide assuming a homogeneous current velocity across the channel. Water level changes at shorter intervals were deemed to generally be below the measurement uncertainty and measurements at finer spatial scales than 2 m did not improve the accuracy of the flow estimate. Surface water discharge out of the wetland was estimated by multiplying wetted area per unit time by current velocity and integrating over time.

2.3 Radon in surface water

Radon time series measurements were conducted over the course of the fieldwork in the tidal channel at the wetland outlet (Figure 1). Surface water was pumped from 0.2 m beneath the water surface at a rate of 2.5 L/min into an air-water exchanger that allowed the radon concentrations in air and water to equilibrate. Through a closed air loop system (Burnett and Dulaiova, 2003), the air was then pumped into a radon detector (RAD7) which measured radon concentrations every 30-min by detecting the α-emitting daughters of radon, $^{214,\ 218}$Po (Dulaiova et al., 2005). The radon concentration in water was calculated based on the gas solubility incorporating the effects of water temperature and salinity (Schubert et al., 2012). A

30 minute lag time correction, which is required for radon to reach equilibrium using this approach, was applied to the data (Schubert et al., 2012).

2.4 Radon diffusion from sediments and ingrowth

Three sediment samples from the wetland and up to 0.2 m depth were collected, brought back to the laboratory, placed in gas-tight containers with radium-free water (sediment to water ratio by volume = 0.2) and sealed for at least one month for measuring radon molecular diffusion from sediments. The system was regularly mixed by tilting. The water inside the containers was then collected into a 6L gas-tight plastic bottle from the bottom up preventing any effects of heterogeneity within the core for radon measurements using a RAD7 as described above (Lee and Kim, 2006). The principle behind this experiment was that after a month (equal to 6 radon half-lives), the source (emanation and diffusion) and sink (decay) of the radon will reach steady state (secular equilibrium) within the sediment core (Santos and Eyre, 2011). To estimate radon ingrowth from the decay of dissolved radium (^{226}Ra) as radon's parent isotope, 40L containers were used to collect surface water at two low and two high tides. The water was then filtered through a column containing 0.015-0.020 kg manganese oxide impregnated fibre which absorb ^{226}Ra (Moore, 2003). The fibres were sealed and left for at least one month before ^{226}Ra concentration analysis following established procedures (Kim et al., 2001).

2.5 Radon mass balance

Subsurface flow was estimated through a radon mass balance model, developed based on time series measurements of radon following Peterson et al. (2019). The mass balance was calculated for three diel cycles with the final radon-derived subsurface flow calculated as an aggregate of the resulting net flow from each of the diel cycles. The mass balance model considers all known sources of radon (incoming flow, diffusion from sediments, ingrowth from parent isotopes and inputs from porewater) and sinks of radon (outgoing flow, atmospheric evasion and radioactive decay) and assumes the missing radon to balance the model is provided by subsurface flows as follows:

$$Q_{gw}\,{}^{222}Rn_{gw} + Q_{in}\,{}^{222}Rn_{in} + Q_{dif}A + {}^{226}Ra\lambda_{222}V = Q_{out}\,{}^{222}Rn_{out} + {}^{222}Rn\lambda_{222}V + J_{atm} \quad (1)$$

where Q_{gw} is the subsurface flow rate (m^3/s); ${}^{222}Rn_{gw}$ is the groundwater endmember concentration (Bq/m^3); Q_{in} and ${}^{222}Rn_{in}$ are incoming flow (m^3/s) and radon concentration (Bq/m^3) during incoming tide; Q_{dif} is radon diffusive flux (Bq/m^2/s); A is the surface area

(m^2); ^{226}Ra is surface water radium concentration; λ_{222} is radon decay rate (2.09×10^{-6}/s); V is the volume of water in the wetland (m^3); Q_{out} and $^{222}Rn_{out}$ are outgoing flow (m^3/s) and radon concentration (Bq/m^3) during outgoing tide; J_{atm} is radon atmospheric evasion (Bq/s).

Radon atmospheric evasion fluxes were calculated using the empirical gas exchange equation for tidal environments proposed by (Borges et al., 2004):

$$J_{atm} = k_g\left(^{222}Rn_w - \alpha\,^{222}Rn_{air}\right) A \quad (2)$$

where, $^{222}Rn_w$ and $^{222}Rn_{air}$ represent the radon concentration in water and air, respectively; α is the Ostwald solubility coefficient (dimensionless) describing the distribution of radon at equilibrium as the fluid-to-gas ratio; and k_g is the gas transfer velocity at the air-water boundary which is driven by wind, current and water depth in tidal environments. The value of k_g (m/d) was calculated for each time interval using Equations (3) and (4) separately and the sum was used in Equation (2) (Borges et al., 2004; MacIntyre et al., 1995):

$$k_{600wind} = 0.45u^{1.6}(Sc/600)^{-a} \quad (3)$$

$$k_{600current} = 1.719w^{0.5}h^{-0.5} \quad (4)$$

where $k_{600wind}$ is the gas transfer velocity driven by winds, u is wind speed (m/s); Sc is the Schmidt number for radon at a given water temperature; and a is a variable power function dependent on wind speeds (a = 0.6 for u < 3.6 m/s, and a = 0.5 when u > 3.6 m/s); $k_{600current}$ is the gas transfer velocity driven by currents, w is the water current (m/s) and h is water depth (m). The Schmidt number (Sc) was determined using formulations from MacIntyre et al. (1995) and ranged from 660 to 3400. During the sampling period, wind speed ranged from 0 to 11 m/s. The area of the entire wetland (113,330 m^2) was used to upscale wind evasions, however, only the estuarine tidal channel area (5,637 m^2) was used to determine current-driven evasions as currents in the intertidal mudflats approached zero.

2.6 Radon in groundwater

Groundwater samples (n=14) were collected from the intertidal mudflat zones during low tides. A hand auger was used to install shallow, 0.05 m diameter PVC pipe piezometers up to depths of 2 m, with 0.5 m long screens. The piezometers were purged three times before collecting a sample using a peristaltic pump. A 6L gas tight Nalgene HDPE (High-density polyethylene) bottle was used to collect and measure radon concentrations in groundwater. Samples were analysed in less than 24 hrs by connecting each bottle to a RAD7 radon monitor device and

running for at least 2 hours to achieve an air-water radon equilibrium with <5% uncertainty following standard protocols (Lee and Kim, 2006).

2.7 Measurement of temperature time series

To gather temperature and water level time series, four representative measurement locations were chosen within the tidal wetland and equipped with T-arrays; T1 to T4 (Figure 1). T4 was placed downstream near the mouth of the tidal channel of the wetland and approximately 5 m from the radon measurement location. T2 was placed upstream, where the wetlands main channel was shallow and narrow. The other two T-arrays were placed in the intertidal mudflats north (T1) and south (T3) of the tidal channel. T4 was continuously inundated, therefore, its setting was similar to measurements in a riverbed (Rau et al., 2014). The other T-arrays experienced variable tidal inundation and exposure, where due to their mud flat locations, T1 and T3 experienced the longest periods of exposure.

The T-arrays were purpose made (Figure 3), each consisted of two PVC pipes 0.032 m in diameter, a ~1.8 m (long) and a ~1 m (short) pipe, respectively. The bottom 0.2 m of the long pipes were screened, with a screen depth of around 1 - 1.2 m below surface, while the short pipes were screened over the entire length. The short pipes were entirely submerged during high tides; the tops of the long pipes were continuously above the highest tidal level and vented to the atmosphere. Single temperature loggers Solinst Levelogger Edge Model 3001 were installed in the long pipes. In the short pipes, Leveloggers were installed to measure surface water temperatures, while additional loggers measured at 5 depths in the sediment. At 0.02 and 0.05 m depth, TidbiT® v2 (UTBI-001) were used. These loggers were small and could therefore be placed close together to measure temperature at narrow depth-intervals near the surface. The three deeper temperature loggers at 0.10, 0.23 and 0.42 m were HOBO® Water Temperature Pro v2 (U22-001). The measurement interval of all loggers was 60 s. To account for potential variations in temperature data due to different logger types, the temperature offsets between loggers were recorded in a water bath and the collected field data corrected for the offset to a common reference.

Field measurements of bulk sediment thermal conductivity (k) and bulk heat capacity (C) were measured using a KD2 Pro Thermal Properties Analyzer field instrument. The thermal properties were measured at different depths in the mudflats (T1 and T3), in the upper part of the channel (T2) and in the deep section of the channel near T4. Thirty-four measurements were performed in total; hence, several values were obtained at each location and depth. For

the heat transport analysis, values presented in Table 1 were applied for each individual T-array.

2.8 Heat transport model

The measured temperature time series were used to estimate vertical exchange fluxes in the tidal wetland by applying combined heat and fluid transport modelling based on the one-dimensional vertical transport solution of Suzuki (1960) and Stallman (1965). They describe the one-dimensional, vertical, anisothermal transport of fluid and heat through homogeneous, porous media as:

$$k\frac{\partial^2 T}{\partial z^2} - q_z C_w \frac{\partial T}{\partial z} = C\frac{\partial T}{\partial t} \quad (5)$$

where k is the thermal conductivity of the soil-water matrix in W/mK, T is the temperature in K, at depth z at time t in the sediment. C_w is the volumetric heat capacity of the fluid in J/m^{3}K, C the saturated volumetric heat capacity of the sediment-fluid matrix in J/m^{3}K, q_z the vertical component of the Darcy velocity in m/s. For convenience, we use the unit of cm/d. A negative q_z corresponds to water flowing from the surface into the sediment (infiltration), while a positive q_z indicates flow from the sediment out to surface (exfiltration).

The analysis of the analytical solution for Equation (5) was conducted with the open-access model environment 1DTempPro (Koch et al., 2016). The physical sediment properties needed for 1DTempPro are bulk k, C and the porosity of the saturated sediment ϕ_s. A porosity ϕ_s of 0.60 was chosen for the site as reported by the NSW Department of Primary Industries (2008).

For the heat conduction and advective transport model the boundary conditions are defined at the interface between surface water and sediment (i.e. a depth of 0.0 m at the uppermost logger of the short pipe) and the location of the deepest logger in the subsurface (located in the long pipe). The other temperature time series are used to fit measured and modelled data. The model was applied to each single high and low tide and integrated over three diel cycles (i.e. the same period as for radon). Most parts of the wetland drained during low tides with visible seepage patterns. It was assumed that although seepage has happened, a saturated sediment profile remains present. The 1DTempPro model calculates and integrates vertical exchange fluxes over the modelled period by changing its value until a minimal difference between modelled and measured subsurface temperature distribution is reached. For presentation purposes, this is

expressed by the Root Mean Square Error (RMSE). The quality of the model output was classified by the average RMSE per T-array and its standard deviation.

2.9 Darcy's flow calculation

The piezometers used for calculating the subsurface flow were the same as those used for groundwater sampling. Water levels were measured every 15 minutes with Solinst Leveloggers placed in each piezometer. The top of all piezometer was surveyed to Australian Height Datum (AHD) using a Trimble 5800 RTK-GPS (real-time kinematic global positioning system), accurate to less than ± 20 mm. The subsurface flow was calculated based on hydraulic heads for time increments of 15 minutes with negative values indicating infiltration and positive values representing exfiltration. Subsurface flow per unit width (i.e., through a 1 m x 1 m area perpendicular to the flow direction) was calculated for each diel cycle separately by integrating the (rising and falling) head gradient data over each diel cycle. The flow calculation was completed for all transects (piezometers A-C, F-D, G-H, J-I, and M-L), and an average calculated. Darcy's Law follows Equation (6) (Darcy, 1856):

$$Q_l = K_{sat} \frac{\Delta H}{\Delta l} A \quad (6)$$

where Q_l is Darcy's (lateral) flow in m^3/d; K_{sat} is the saturated hydraulic conductivity in m/d; ΔH is the difference in the hydraulic heads of the two piezometers in a transect in m; Δl is the distance between the piezometers in m and A is the height determined by the difference between the maximum upper saturated surface and the minimum channel surface elevation per unit width (1 m) for each transect (m^2). The results were upscaled using the length of representative shoreline for each transect. The hydraulic conductivity for coastal wetland mangrove sediments perforated with animal burrows (similar to the study site here) is suggested to range from 1 – 10 m/d (Susilo and Ridd, 2005). Based on hydraulic head gradient measurements in conjunction with heat tracer derived fluxes, a range of vertical hydraulic conductivities of 0.1 to 5 m/d was estimated for the site. Here, based on field data and the literature, a K_{sat} value of 5 m/d was used and the distance between each piezometer was determined in ArcGIS v10.5. Interpolation of hydraulic heads for creating groundwater maps was also prepared in ArcGIS v10.5 using the Inverse Weighted Distance method (Noori et al., 2013).

3 Results

3.1 Surface water time series and groundwater observations

Observed surface water levels indicated a semi diurnal tidal behaviour with water depths ranging from 0.1 to 1.7 m in the estuarine tidal channel entrance of the wetland during measurements (Figure 4). Salinity was mostly at oceanic values (~ 35 ppt) and slightly increased during ebb tides. During the rainfall event, freshening occurred, and surface water salinity dropped to 17 ppt. Surface water temperature ranged between 17.2 to 29.4 °C and generally decreased at low tide. Flow velocity in the estuarine channel reduced at low tide and varied between 0.002 to 0.09 m/s. Radon followed a trend opposite to the tides with concentrations increasing at low tide and decreasing at high tide, ranging from 20 to 850 Bq/m^3.

Groundwater in the wetland was hypersaline and salinity varied between 42.1 to 51.7 ppt across the wetland (Table 2). Median groundwater temperature was 22.5 °C, which was one degree lower than median surface water temperature. Radon in groundwater varied between 710 to 1060 Bq/m^3 with a median of 882 ± 104 (1 SD), which was similar to radon concentrations in the surface water at low tide (when maximum seepage is expected). Median radon concentrations in groundwater were 2-folds greater than those observed in the surface water.

3.2 Radon mass balance model

Surface water radon concentrations from the channel entrance at each measured time interval were multiplied by surface water discharge for the same time interval and integrated over three diel cycles. Based on the radon mass balance of measured sources and sinks, it was found that tidal flow out of the system within each of diel cycles was the major radon loss, and on average accounted for over 60% of total radon losses (Table 3). On average, over the three diel cycles wind evasion, accounted for 30% of total losses and the remaing loss was due to current evasion and radon radioactive decay (Table 3). The average calculated gas transfer velocity was 2.2 ± 0.8 m/d.

The most important source and sink of radon withing the system (wetland) was from tidal flows (ebb and flood), indicating tides were the major driver of radon changes in the system. For example, the radon source to the wetland during flood tide were an order of magnitude higher than radon inputs from sediment diffusion and radon ingrowth, indicating that advective flow was the dominant process in the system. Molecular diffusion rates from wetland sediments were small (5.2 ± 1.5 Bq/m^2/d) and after upscaling to the whole wetland area accounted for

less than 4% of all radon sources. Radon ingrowth from its parent isotope (Ra-226) was the smallest radon source.

The missing radon source to balance the equation was assumed to be porewater inputs and was estimated by dividing the missing radon flux by the radon concentration in groundwater. This resulted in a volumetric average subsurface flow of 0.13 ± 0.05 m^3/s over the three diel cycles. Considering the wetland area (113,330 m^2), the subsurface flow was estimated to be 10.2 ± 4.2 cm/d on an areal basis (Table 3). Over the three diel cycles, results showed the highest net flow was during the 3rd diel cycle with an exfiltration of 4.9 ± 2.2 cm/d while the lowest net flow was during the 2nd diel cycle (2 ± 0.8 cm/d) coinciding with the rainfall event (Figure 5).

3.3 Measured water temperatures and heat tracer analysis

Figure 6 presents the range of measured surface and groundwater temperatures per T-array during the sampling period. The temperature envelopes were drawn by connecting the maximum, minimum and average temperatures measured per depth. T4 located at the estuarine channel (wetland entrance) was constantly inundated and showed the smallest temperature range, visible near the surface-sediment interface (i.e., 0.0 m). The surface water temperature ranged from 17.1 °C to 33.8°C. For the other T-arrays a temperature maximum of 36.8°C was measured at T2 and a minimum of 12.0°C at T3. While the temperature variation near the surface was very high, it reduced strongly with depth. Below 0.23 m depth, temperature varied less than 3°C. At the deepest measurement location, around 1 - 1.2 m below surface a maximum temperature of 21.0°C and a minimum of 19.2°C was observed. While average temperatures are similar between T1 - T3, T4 had higher average temperatures.

Figure 5 shows the heat tracer derived vertical water exchange fluxes per diel cycle as vertical bars. The results show temporal heterogeneity with values varying from an exfiltration fluxes of 13.9 cm/d during the 1st diel cycle to infiltration fluxes of -18.8 cm/d during the 3rd diel cycle. While the exfiltration fluxes from the heat tracing method remain almost constant during the three measured diel cycles (Figure 5b), the infiltration fluxes increase (Figure 5a). The net flux during the 1st diel cycle is positive at 7.8 cm/d, but gradually shifts to a negative value of -6.2 cm/d in the 3rd diel cycle (Figure 5c).

The heat tracer derived results were spatially extrapolated by assuming relative homogeneity across the wetland and assigning each T-array to a representative part of the wetland to calculate volumetric subsurface flows. The assigned areas covered 5,637 m^2 for T4 and 44,334

m^2 for T3. T1 and T2 cover 23,380 and 39,949 m^2, respectively. Since T4 represented only the permanently inundated parts of the wetland, its area was limited to the main channel. During the three diel cycles a volumetric exfiltration of 33,919 m^3 and an infiltration of 21,480 m^3 was calculated, resulting in a total exfiltration of 12,439 m^3. Summing up over the three tidal cycles a net exfiltration of 4,032 ± 3,286 m^3/d for the entire wetland was calculated, equivalent to a vertical net subsurface flow of 4.3 ± 2.9 cm/d (Table 4).

3.4 Darcy's flow results

Hydraulic head in piezometers closest to the centre of the wetland (i.e., C, H, L, I, D) varied in a similar way following the tidal trend, whereas piezometers located furthest away from the centre of the wetland (i.e., A and F) did not show significant variation (Figure 4; heads in Piezometers A and C are shown as representative). Figure 7 shows groundwater flow maps for the highest and lowest tide during the measurement period. During the highest tide, hydraulic gradients were away from the central tidal channel and towards the fringes of the wetland, indicating water being transported from the Hunter River into the wetland via the central channel and then further distributed onto the mud flats (Figure 7a). During the lowest tide, the hydraulic gradients reverse and point towards the central tidal channel, where subsurface water is drained (exfiltration) from the mud flats and transported out of the wetland via the central channel (Figure 7b). Due to the topography, tidal waters did not affect water levels in piezometer F, creating a reducing gradient from this piezometer towards the south channel of the Hunter River during both high and low tide.

Based on applying Darcy's equation to the head data the highest net flow per unit width was from the transect of piezometers G – H, which also had the largest exfiltration at the lowest tide during the sampling period (Table 5). The smallest net flow per unit width was from piezometers E – D. Overall, estimated flows using Darcy's equation showed nearly equal infiltration and exfiltration during each of the diel cycles over the sampling period resulting in small net flows. The highest infiltration and exfiltration over the sampling period occurred during the 3rd diel cycle and were -3.8 ± 2.0 and 6.2 ± 2.9 cm/d, respectively, as illustrated in Figure 5. The average net flow per unit width from all piezometer transects was an exfiltration of 3.2 ± 1.8 cm/d which resulted in a volumetric flow of 792 ± 420 m^3/d. The resulting flow from Darcy's equation was ~70% of those estimated from heat tracing and 30% of the flow calculated using the radon tracer.

4 Discussion

Limitations associated with each field method and their uncertainties arising as a consequence are explained below. The dataset and subsurface flow processes occurring at the wetland, as well as how each method captures these processes, is then detailed. The implications of the study regarding solute transport in coastal environments are also discussed.

4.1 Uncertainty and limitations of measurements

4.1.1 Radon tracing

The radon endmember concentration in groundwater is usually considered as the dominant source of uncertainty in a radon mass balance approach. Radon concentration can vary significantly over a small spatial scale and previous studies have used from 5 to 40 samples to determine the radon endmember concentration (Peterson et al., 2008; Su et al., 2014). Here, we collected 14 groundwater samples spatially distributed across the site and located < 1 km from the estuarine time series station to represent the groundwater radon composition at the wetland following recommendation from Sadat-Noori et al. (2015). The median radon concentration (882 ± 104, 1 SD) in groundwater samples was used as the endmember in the mass balance to calculate the radon-derived subsurface flow. The error associated with using this median concentration (i.e., the standard error of all groundwater measurements) is propagated through the subsurface flow calculations to highlight the uncertainty associated with this approach. If the minimum radon groundwater endmember (lowest value measured) was used, the exfiltration flow would increase by 25% and if the maximum radon groundwater endmember was used, the exfiltration would decrease by 16%.

As radon is a gas, quantifying losses through wind evasion can also be a source of uncertainty in the mass balance model (Dulaiova and Burnett, 2006). Determining the gas transfer velocity (K_g) through empirical gas exchange equations in dynamic coastal estuarine areas is often associated with some level of uncertainty (Burnett et al., 2007). Here, we apply the most widely accepted gas exchange equation for estuarine environments in the literature (Borges et al., 2004). The way in which wind speed data is incorporated into the overall radon wind evasion can also affect the results. There is discrepancy in the literature regarding the best method to represent wind speed for radon wind evasion estimates. Previous studies have suggested using average wind speed data covering the sampling period (Dimova et al., 2013), or averaged wind speed data from 5–10 days before sampling to account for the cumulated effect of evasion from the waterbody (Gilfedder et al., 2015). In this study, we use average daily (24 hrs cycle) wind

speeds. If average daily wind speeds for a longer period (e.g., 10 day) was used, no significant changes in radon wind evasion would occur (i.e., resulting in similar subsurface flow rate) as the variations in wind regime in the 10 day period before sampling was similar to the 24 hour period before sampling. Sampling for longer periods and/or several seasons could provide further insight in the variability of the groundwater-surface water interaction processes. However, the long-term deployment of such instrumentation is logistically and technically challenging.

4.1.2 Heat tracing

Three sources of error were investigated as part of the heat tracer analysis, i) influence of model parameters, ii) vertical uncertainty of the logger depth and iii) model fit. For i) estimation errors on k of ± 0.1 Wm/K and on C with ± 0.3×10^6 J/m^3/K were assumed. The average influence on the flux results was 1.2 cm/d. The error of a vertical misplacement of the T-arrays of ± 2 cm yielded an error in the flow of 1.7 cm/d. The obtained errors were proportional with fluxes; hence, higher errors were found for higher fluxes. The integration of errors yielded ± 2.9 cm/d which was assigned to all calculated fluxes, which is probably overstating the actual errors.

Most heat tracing methods assume strictly 1D vertical flow within a homogeneous subsurface material. Natural sedimentary systems are usually a heterogeneous and layered structure (Karan et al., 2013). In the investigated tidal wetland, crab borrows and old root channels up to > 0.1 m in diameter may have added preferential flow paths that cannot be simulated with point measurements and an assumption of homogenous conditions. Additionally, even with perfect homogeneous conditions, subsurface flow fields are 3D (Zlotnik and Tartakovsky, 2018). Hence, the predominant flow direction in the wetland may not be vertical or may shift in time from vertical to a more lateral direction. Such a behaviour could influence both the flux estimate and the volumetric flow calculation (Ferguson and Bense, 2011; Lautz, 2010).

A further model assumption is a constant exchange flow during the modelled period, while the exchange flow in the tidal wetland is thought to be variable in time. The superposition of diurnal and tidal thermal signals may also influence the modelling results. A model code like 1DTempro suffers from initialisation errors. The subsurface temperature distribution at the start of the modelled time series is a linear interpolation of the measured starting values, while the natural temperature distribution contains temperature information prior to the measurement.

4.1.3 Head gradients (Darcy's flow)

The largest uncertainty in the Darcy flow calculations is the assignment of a value for hydraulic conductivity. The value used in our study is derived from onsite head gradient measurements and the literature, and we assign an uncertainty of 50% to the K_{sat} value used in the calculations to account for potential errors associated with hydraulic conductivity. If we use the higher end estimate of a K_{sat} value of 10 m/d in our study (from the literature), maximum exfiltration and infiltration fluxes would increase however, the resulting net flux would not change significantly (3.8 ± 2.3 cm/day) due to the integration of exfiltration and infiltration fluxes. An additional source of error in using Darcy's equation could be related to defining the subsurface cross-section area of the flow. We account for this in our estimation by assigning an uncertainty of 10% to both the length, and the width of the cross-sectional area. Further detailed geological studies would be required to get a better understanding of the subsurface cross-sectional area for the study site.

4.2 Radon dynamics and related exchange fluxes

Radon accounts for total groundwater exchange (i.e., fresh and saline; terrestrial and recirculated) as salinity has little or no effect on radon concentrations in groundwater (Douglas et al., 2020). Radon concentrations followed a clear tidal trend with high radon activity at low tide indicating groundwater exfiltration occurred at low tide mainly driven by the pressure gradient difference between groundwater and surface water levels at low tide (Figure 4). This is a common trend observed by others in coastal settings (Davis et al., 2020; Webb et al., 2019). In such cases, a significant inverse relationship between porewater exfiltration and tidal height is expected (Call et al., 2015; Sadat-Noori et al., 2017), as was also observed here (Figure 8) confirming that groundwater exfiltration was mostly driven by tidal pumping (Figure 4).

Figure 5c showed the lowest net flow occurred during the 2nd diel cycle which was caused by a shorter peak in surface water radon concentrations. This in turn, was due to radon dilution with rainwater during the time of the rainfall event (Figure 4). Although the rainfall event could have influenced the subsurface flow, the highest net flow observed in the 3rd diel cycle was most likely attributed to tidal range with larger peaks (compared to previous tides) causing a higher gradient between groundwater and surface water, as the radon tracer was mainly driven by the tidal dynamics.

4.3 Measured temperatures and related exchange fluxes

During the three diel cycles the temperature influence of tidal and radiation effects can be observed up to a depth of 0.05 m but do not affect any temperature measurements at 0.10 m and below (Figure 4). Compared to T2 and T4, T1 and T3 show a strong temperature variation near the surface, but the envelopes are narrower below 0.1 m depth, and, hence, indicate less temperature variation in depth. While the average temperatures for T1, T2 and T3 are very similar (Figure 6), T4 shows higher average temperatures. These results indicate the transport of heat from the land surface into the sediment during measurements. Two phenomena may account for this namely, i) a different sediment composition with higher thermal conductivity and lower heat capacity as indicated in Table 1, and/or ii) lower exfiltration or higher infiltration fluxes.

Similar patterns of surface and groundwater temperatures were observed at another tidal location by Halloran et al. (2017), which in comparison to temperatures time series measured in rivers are considerably more complex (Anibas et al., 2016). Driven by solar radiation, diel temperature changes at the lands surface follow a sine function, where during the day it heats up and during the night it cools down. As they are also strongly influenced by tides (Figure 4), temperatures in a tidal wetland generally do not follow a sine wave. The non-stationary water levels in the wetland influences the subsurface temperatures. During high tides, high water levels dampen and delay subsurface temperature changes, indicated by slower temperature rises during day, and a delayed cooling during night. High tides transport water from the Hunter River Estuary and, hence, its heat energy into the wetland, which increases or decreases its subsurface temperature, respectively. For example, high tides during night can create a temperature peak. During low tides diel temperature changes are translated fast into the subsurface due to the decreasing heat capacity of the remaining water, and eventually due to direct solar radiation on the sediment surface when not inundated.

The heat-derived vertical net subsurface flow of 4.3 ± 2.9 cm/d was less than radon-derived estimates but higher than Darcy's flow. Heat tracer-derived results indicate an increase in vertical infiltration flux over the three diel cycles, while the exfiltration remains constant (Figure 5). This leads to a change from net exfiltration to a net infiltration during the three diel cycles. This could be a consequence of the tidal range becoming larger towards the end of the measurement period (e.g., approaching spring tide). The rainfall event shortly prior to the 3rd diel cycle could also be responsible for this change in flow direction measured by the heat

tracing method. The rainfall could have temporally affected (i.e., increased) surface water levels and caused infiltrating conditions. However, the heat tracer derived flux results and their spatial upscaling yielded comparable values to the radon tracer experiment and Darcy's flow calculations. This clearly indicates the applicability of heat tracing in such highly dynamic environments as tidal wetlands. The analysis of longer temperature timeseries measurements could reduce potential uncertainties in the quantification of subsurface flow using heat tracer in tidal wetlands.

4.4 Subsurface flow source: recirculated seawater or regional flow?

Regarding the magnitude and direction of subsurface flows, the results of the three methods complimented and validated each other. The values obtained with the three methods agreed within an order of magnitude. Hence, the combination of methods increased the confidence in the flux calculations. Additionally, this combination assisted in quantifying various flux processes (explained below) compared to a single method, thereby providing a more holistic image of the system and its subsurface flows. The three methods applied for this study provided different subsurface flow rates, although all were within a similar range and indicative of net exfiltration during the study period (Table 6). While the net subsurface flow over the sampling period (three diel cycles) was positive (exfiltration), on shorter time scales, e.g., during individual high and low tides, flow direction changed from exfiltration to infiltration. Overall, the system had a net discharge, meaning that water was leaving the catchment mainly due to the general seaward gradient.

The radon-derived flow represented the total subsurface flow to the wetland over the sampling period. Flows estimated from the heat and Darcy's equation equated to 42 and 30% of the radon-derived flow, respectively. Other studies using multiple environmental methods to quantify subsurface flow in wetlands/lakes have also reported Darcy's equation producing the lowest flow rates compared to heat and isotope methods (Hunt et al., 1996; Mulligan and Charette, 2006; Su et al., 2016). Here, we interpret the Darcy-derived flow as mainly lateral subsurface flow and flow from heat tracing as vertical flow as the measurements are being done either along a predominantly horizontal plane or vertical plane, respectively. Radon incorporated both (total) flows over the sampling period. The difference in the estimated flows is likely because radon takes into account the discharging recirculated surface or seawater, in addition to regional subsurface flows from the adjacent wetlands, whereas the Darcy calculation ignores the contribution from vertical gradients (i.e., vertical upward gradients

during low tide discharge). The difference in fluxes can also indicate the influence of crab burrows and roots canals in increasing the porosity in the wetland's sediments which is not accounted for by heat tracing and head gradient methods. Figure 9 illustrates a conceptual model of the processes occurring and measured by each method at the wetland.

Although the differences between the estimated fluxes are thought to be due to the vertical and horizontal orientation of the heat and head methods, respectively, the spatial scale of measurements can also explain part of these differences. It is possible that exfiltration does not happen equally across the site due to spatial heterogeneity. Discharge can be high at certain locations where a narrow seepage face exists, and consequently lower elsewhere. The small-scale heat and head installations may be localised and overlook exfiltration hotspots elsewhere on the tidal flat. However, radon integrates over the entire wetland, including all zones of high and low flow. The comparison of the three methods in Table 6 indicate that the radon method provides a total discharge that is two to three times larger than the discharge estimated by the heat and head methods, respectively. This could indeed indicate that some seepage hotspots are not detected by the heat and head measurements. While no information on the width of the seepage face is available for this wetland, investigations elsewhere have shown seepage faces in the range of 1 - 200 m (Taniguchi et al., 2003).

Surface water flow measurements at the entrance of the wetland indicated a net surface water discharge of 0.6 m^3/s over the sampling period. Based on the subsurface flow estimates derived by the radon tracer, which represented the total subsurface flow (0.13 m^3/s), subsurface flow contributed about 20% to the surface water exiting at the mouth of the wetland over this period. This includes all subsurface flows, from recirculated surface water (seawater) to regional fresh groundwater discharge leaving the catchment. We assume the flow estimated by Darcy's equation only represents the lateral regional subsurface flow and hence, if subtracted from radon-derived flow, the remaining is likely to represent the recirculated surface water exchange. This is defined as water that infiltrates the wetland during the flood tide and exchanges back out again during the ebb tide. Based on this approach, the different components of the subsurface flow were separated and the contribution of the recirculated surface water component to the total subsurface flow leaving the wetlands was estimated to be 70% (Table 6). Previous studies have shown that the recirculation component of the overall discharging subsurface flow in various coastal settings (including tidal estuaries) can be significant (Andersen et al., 2007; Beebe and Lowery, 2018; Hays and Ullman, 2007; Sadat-Noori et al., 2016a).

4.5 Implications for dissolved material transport

As coastal wetlands are amongst the most productive ecosystems on earth, flow discharging from their sediment acts as a source and pathway for transporting solutes such as nutrients, carbon, trace metals and any other dissolved chemical into coastal waters (Porubsky et al., 2014). On a global scale, studies have shown that nutrient delivered to coastal waters through subsurface flow can rival those delivered by rivers (Cho et al., 2018). Additionally, studies from Asia (Hwang et al., 2005), North America (Su et al., 2014), Europe (Leote et al., 2008), Australia (Makings et al., 2014), and the Mediterranean (Rodellas et al., 2015), have linked coastal water eutrophication to dissolved chemicals delivered by subsurface flow. This subsurface flow can either be meteoric regional groundwater or recirculated surface (sea) water, each having different chemical signatures and nutrient loads (Moore, 2010). Therefore, it is important to separate and accurately estimate these two flow components as this is essential for understanding their effect on the function and maintenance of coastal ecosystems (Burnett et al., 2001; Weinstein et al., 2011).

Solute or dissolved chemical transport from sediments is usually estimated by multiplying the endmember concentration of the chemical in groundwater by the discharging subsurface flow rate (Beck et al., 2015) with the latter part playing a significant role in the overall flux estimation. The three methods used here had inherent differences and quantified overlapping physical processes however, this allowed for distingushing the two components of the discharging subsurface flow within the system. In studies focuing on biocgeochemical cycles and element budgets, such information will contribute to better understanding the export flux of dissolved matter, which has implications for quantifying coastal wetland chemical budgets such as for carbon and nitrogen (Moore, 2006; Santos et al., 2019). In this study, the resulting discharge estimates show that a variety of methods are needed to understand subsurface flow regimes across the land–water boundary in coastal wetlands and quantify sediment solute transport.

5 Conclusions

This study relied on three independent methods including head gradients and two natural groundwater tracers, radon and heat, to quantify subsurface flow in a coastal tidal wetland. The simultaneous application of the three techniques in a tidal environment revealed that results from the radon mass balance were ~3-folds larger than the heat tracing technique and those

calculated by hydraulic gradient. We highlight that these differences are thought to be driven by the different nature of the methods and by method-specific sources of bias, but more important that each method measures separate parts of the system. While radon accounted for the total subsurface flow (terrestrial regional flow and recirculated seawater), head gradients represented lateral flow exfiltrating into the wetland surface water. On the other hand, heat tracers presented vertical subsurface flows. Solely relying on head gradients or heat may underestimate the flow rate and consequently the solute flux transported from tidal wetland to coastal waters. However, using heat or head methods provides additional valuable information to determine the terrestrial component of the subsurface flow. Radon measurements do not allow for high resolution temporal flux estimates, which heat and head methods are capable of producing. Our work has implication for subsurface flow quantification in tidal environments as subsurface flow in tidal wetlands can significantly control the transport of dissolved matter to surface water via different pathways.

In the future, we recommend improving the robustness of field studies based on the methods employed in this study by increasing the spatial density of measurement points and longer field deployments to extend the observation periods. It should be noted that this is usually constrained by the budget and availability of personnel. For example, having an additional radon measuring station located at the upstream parts of the wetland (in addition to one at the mouth) would allow for dividing the wetland into two compartment and thereby disaggregating the measurements. This would help reducing some of the uncertainties when developing the radon mass balance model. Deploying two piezometers next to each other with screens at different depths can provide measurements of vertical hydraulic gradients and the vertical subsurface flow using Darcy's equation (if the hydraulic conductivity is also measured). Longer observation periods would provide a wider range of conditions and natural variability regardless of the method. In particular, longer periods of temperature observations (e.g., >1 month) would reduce data inversion uncertainties associated with this method. Overall, a robust assessment of subsurface flow at any tidal wetland requires a combination of several methods.

6 Acknowledgments

Funding for this research was provided by UNSW Sydney and Newcastle Coal Infrastructure Group (NCIG). We would like to acknowledge Philip Reid and Hayley Ardagh from NCIG for providing logistical support and access to the site. We also thank Sina Alaghmand for his contribution during the fieldwork. Thanks to Anna Blacka, the graphical designer at UNSW, Sydney, Water Research Laboratory (WRL), for assistance in figure preparation.

Table 1. The measured thermal parameters *k* and *c* of the mudflats (T1 and T3), the upstream part of the estuarine channel (T2) and the downstream part of the estuarine tidal channel (T4). For T1, T2 and T3 two measurements in depth were performed, creating individual values for 0.3, 0.4 and >0.4 m of the sediment profile. An increasing trend of *k* is visible between the mudflats and the channel, as well as with depth. An inverse correlation between *k* and *c* is observed.

T-array	Depth (m)	Thermal conductivity *k* (W/mK)	Volumetric heat capacity ***c*** ($MJ/m^3/K$)
T1, T3	0.0-0.4	0.99	3.5
T1, T3	>0.4	1.18	3.3
T2	0.0-0.3	1.10	3.7
T2	>0.3	1.31	3.1
T4	>0.0	1.52	3.0
Average		1.05	3.4

709 **Table 2.** Groundwater depth, salinity, temperature, and radon observations.

Piezometer	Depth (m)	Salinity (ppt)	Temp (°C)	Radon (Bq/m^3)
A	1.5	51.3	23.7	1060
B	1.2	48.3	22.6	950
C	1.1	48.2	21.2	790
D	1.1	46.5	21.5	850
E	1.3	45.9	22.7	820
F	1.4	50.2	23.5	910
G	1.3	53.4	23.8	985
H	1.2	51	24.4	879
I	1.2	51.2	21.2	994
J	1.2	42.1	21.8	980
K	1.3	49.4	20.1	810
L	1.2	48.4	22.3	710
M	1.0	51.7	22.3	725
N	1.3	47.4	24.6	884
	Average	48	22	882
	Std Dev.	3	2	104

710
711

712 **Table 3.** Radon mass balance parameters and the resulting radon-derived subsurface flow
713 over three diel cycles. All radon source and sink units are in Bq/s.

	Parameters	Radon flux	Contribution (%)
Sinks			
	Radon decay	8.8 ± 1.5	2.7
	Wind evasion	98.5 ± 42.5	30.1
	Current evasion	15.4 ± 5.9	4.7
	Radon outflow	205.1 ± 98.2	62.6
	Total radon outputs	327.7 ± 107.2	100
Sources			
	Diffusion from sediments	5.2 ± 2.1	1.6
	Radon ingrowth from ^{226}Ra	6.2 ± 1.7	1.9
	Radon inflow	198.1 ± 58.4	60.4
	Missing radon (groundwater)	188.3 ± 56.5	36.1
	Total radon inputs	327.7 ± 81.4	100
	Subsurface flow (m^3/s)	0.13 ± 0.05	
	Subsurface flow (cm/d)	10.2 ± 4.2	

714

715

716 **Table 4.** Time averaged vertical subsurface flow derived from the 1DTempPro simulations for
717 each T-array and as a summation. The values are weighted by the respective wetland areas.
718 Note that a positive sign (+) indicates groundwater exfiltration.

T-array	Location	Area (m^2)	Vertical groundwater flux (cm/d)	Net groundwater volumetric flux ($m^{3/}d$)
T1	Mudflats north	23,380	+ 7.3 ± 2.9	+ 1706 ± 678
T2	Channel upstream	39,949	+ 2.6 ± 2.9	+ 1039 ± 1159
T3	Mudflats south	44,334	+ 2.3 ± 2.9	+ 1003 ± 1286
T4	Channel downstream	5,637	+ 5.0 ± 2.9	+ 385 ± 164
Total		113,330	+ 4.3 ± 2.9	+ 4032 ± 3286

719

720

721

722 **Table 5.** Subsurface flow estimated using Darcy's equation per unit width for each
723 piezometer transect.

Parameter	Diel cycle	Piezometers A - C	Piezometers E - D	Piezometers G - H	Piezometers J - I	Piezometers M - L	Average flow for all piezometer transects (cm/d)
Net ΔH (m)	1st	0.32 ± 0.02	0.15 ± 0.01	0.25 0.15 ± 0.01	0.20 0.15 ± 0.01	0.18 0.15 ± 0.01	
	2nd	0.41 ± 0.02	0.19 ± 0.01	0.32 ± 0.02	0.24 ± 0.01	0.24 ± 0.01	
	3rd	0.52 ± 0.03	0.18 ± 0.01	0.42 ± 0.02	0.23 ± 0.01	0.28 ± 0.01	
Distance ΔL (m)		87 ± 10	32 ± 3	34 ± 3	37 ± 4	41 ± 4	
K_{sat} (m/d)		5 ± 2.5	5 ± 2.5	5 ± 2.5	5 ± 2.5	5 ± 2.5	
Flow (cm/d)	1st	1.8 ± 0.74	2.3 ± 0.94	3.7 ± 1.47	2.7 ± 1.08	2.2 ± 0.90	
	2nd	2.4 ± 0.94	3.0 ± 1.19	4.7 ± 1.88	3.2 ± 1.30	2.9 ± 1.16	
	3rd	3.0 ± 1.20	2.8 ± 1.13	6.2 ± 2.47	3.1 ± 1.47	3.4 ± 1.37	
Average flow over the three diel cycles (cm/d)		2.4 ± 1.66	2.7 ± 1.88	4.9 ± 3.36	3.0 ± 2.09	2.8 ± 1.97	3.2 ± 1.8

724

Table 6. Net subsurface flow estimated over three diel cycles using multiple methods and the contribution of subsurface flow to net total surface water discharge out of the wetland.

	Flow (cm/d)	Volumetric flow (m^3/s)	Subsurface flow contribution to surface water discharge (%)	Recirculated seawater contribution to subsurface flow (%)	Regional flow contribution to subsurface flow (%)
Surface water		0.6	-	-	-
Radon	10.2 ± 4.2	0.13 ± 0.07	22	70	30
Heat	4.3 ± 2.9	0.05 ±0.04	9	-	-
Darcy	3.2 ± 1.8	0.016 ± 0.01	3	0	100

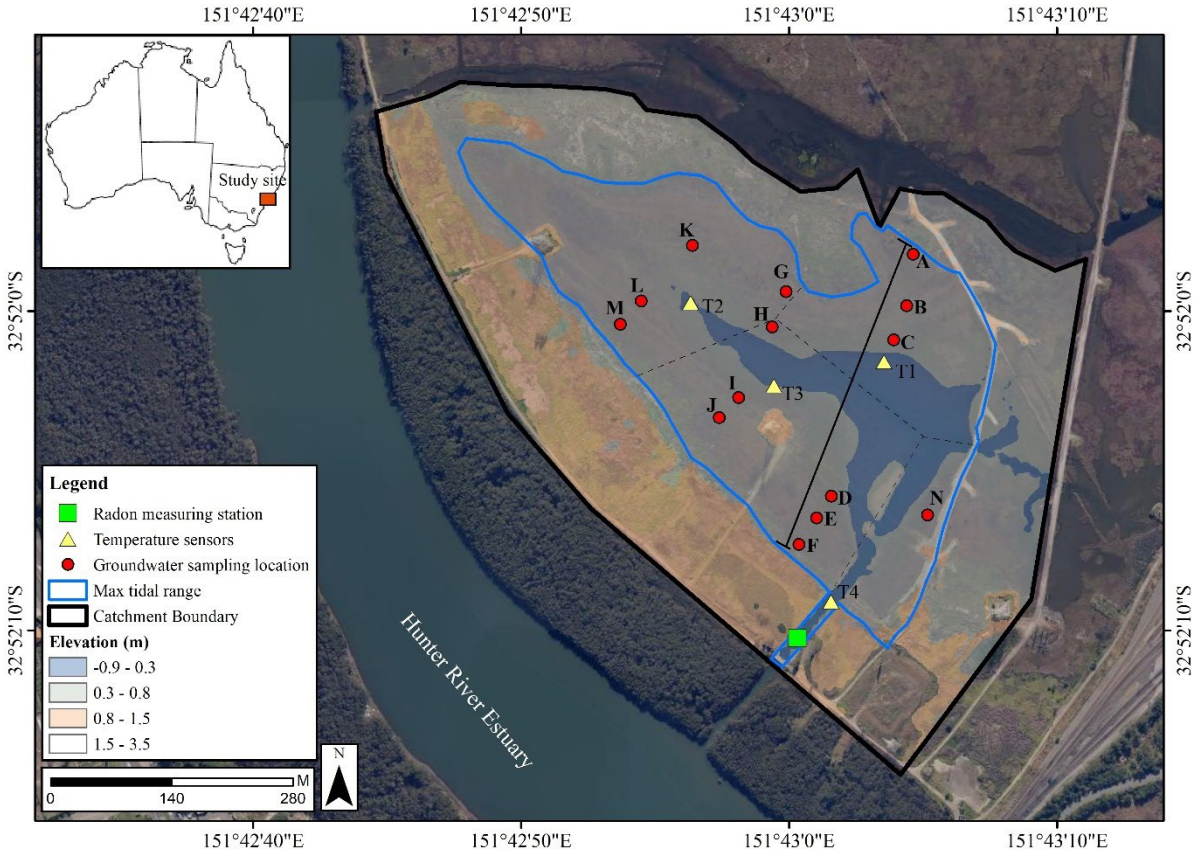

Figure 1. Map of the study area showing the position of the T-arrays 1-4 and the location of the continuous radon measurement. The dark solid line indicates the cross-section location illustrated in Figure 9 covering Piezometers A to F.

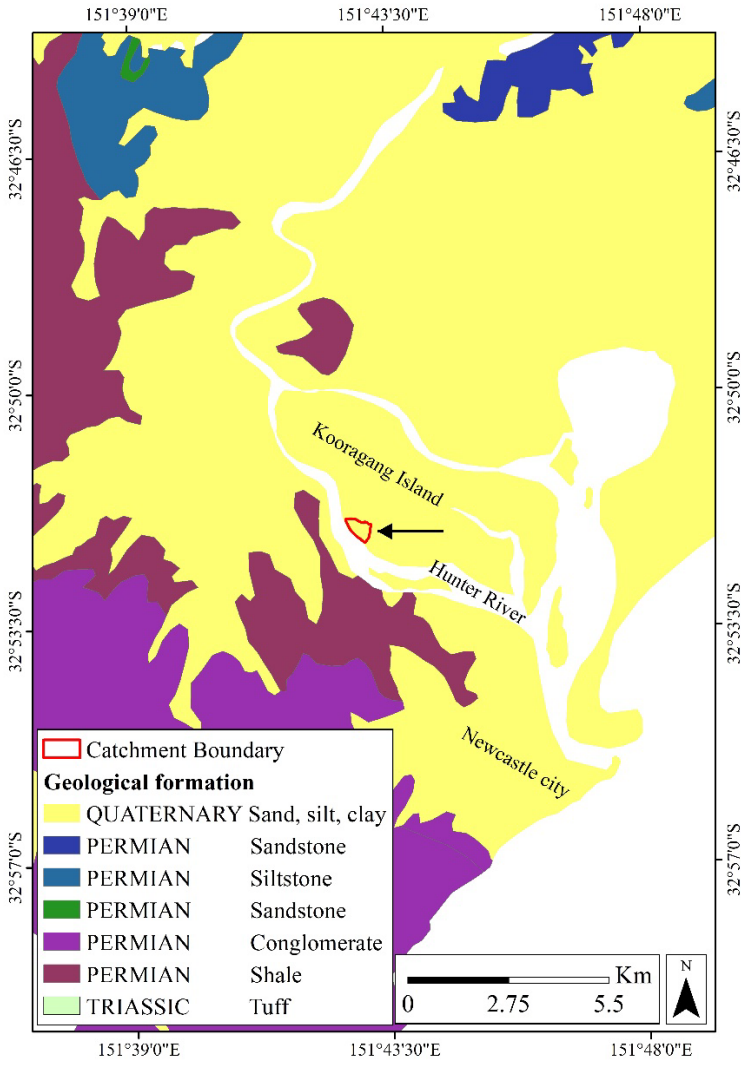

736

737 **Figure 2.** The hydrogeological map of the region showing the entire study area is
738 characterised as quaternary deposits including sand, silt and clay.

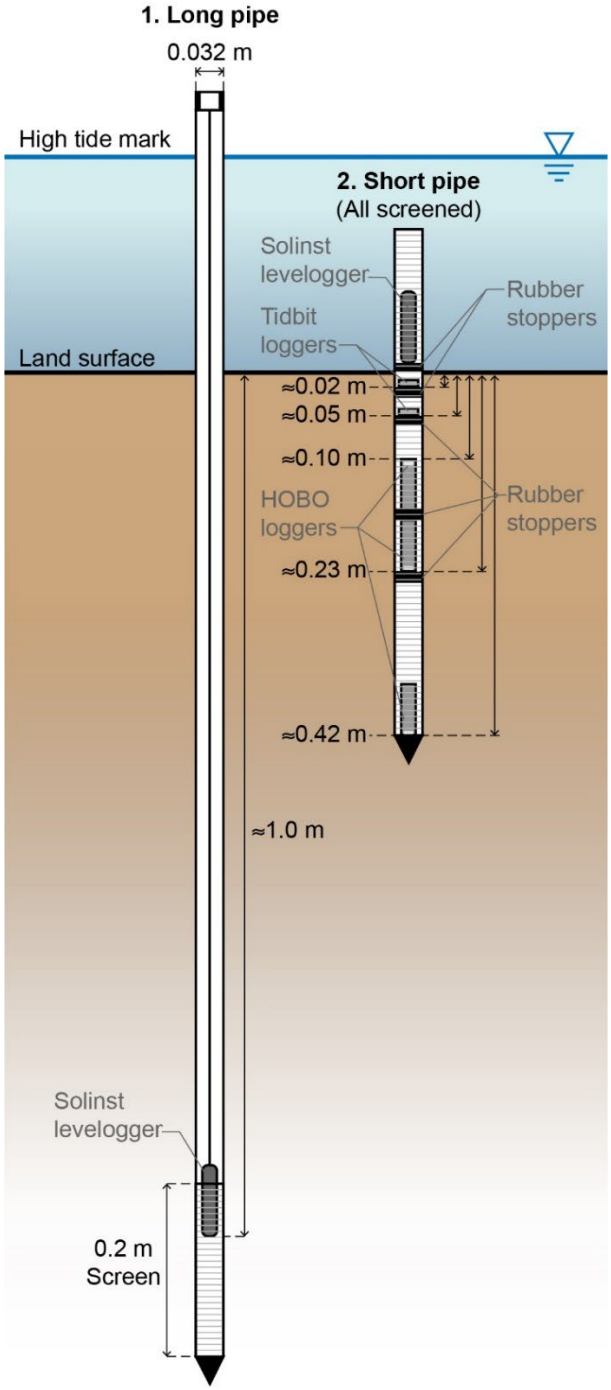

739

740 **Figure 3.** Schematic view of a T-array installed in the tidal mudflats and the estuarine channel.
741 The T-array consisted of two PVC pipes, a vented long pipe measured groundwater
742 temperature and head, 1.0 m below surface. A short pipe completely inundated during high
743 tides measured surface water temperature and groundwater temperatures at several depths
744 below the interface and head at the sediment surface.

745

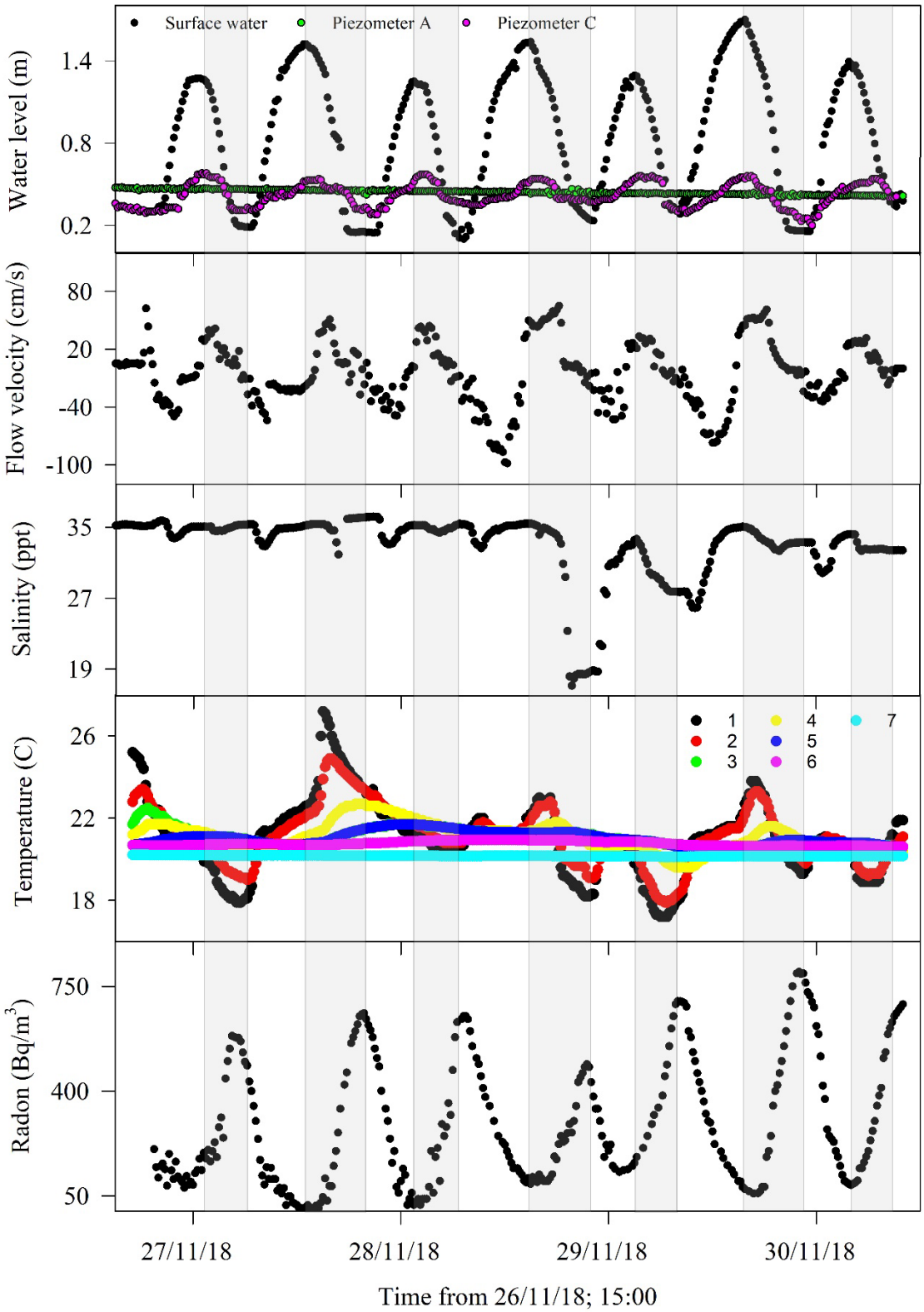

Figure 4. Surface water time series observations at the entrance of the wetland. Groundwater level times series for Piezometers A and C is also shown. Shaded areas indicate low tide periods. Temperature arrays show data for the 7 loggers in T4 T-array with depths of 0.02, 0.05, 0.1, 0.23, 0.42, 1.2 m.

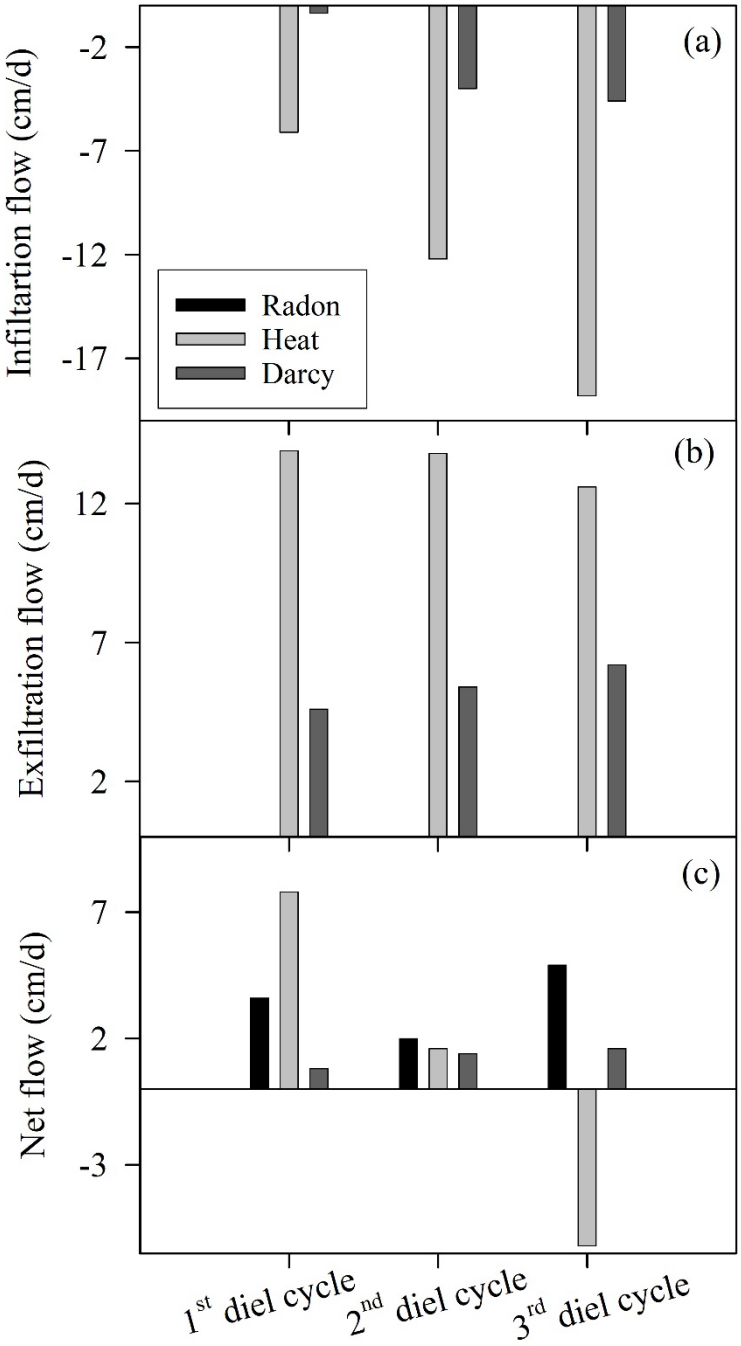

Figure 5. The (a) infiltration, (b) exfiltration and (c) net subsurface flow during each diel cycle over the sampling period based on the methods used. (The radon method only produced net flow). Positive values indicate exfiltration and negative values infiltration. Notice the variable scale of the vertical axes.

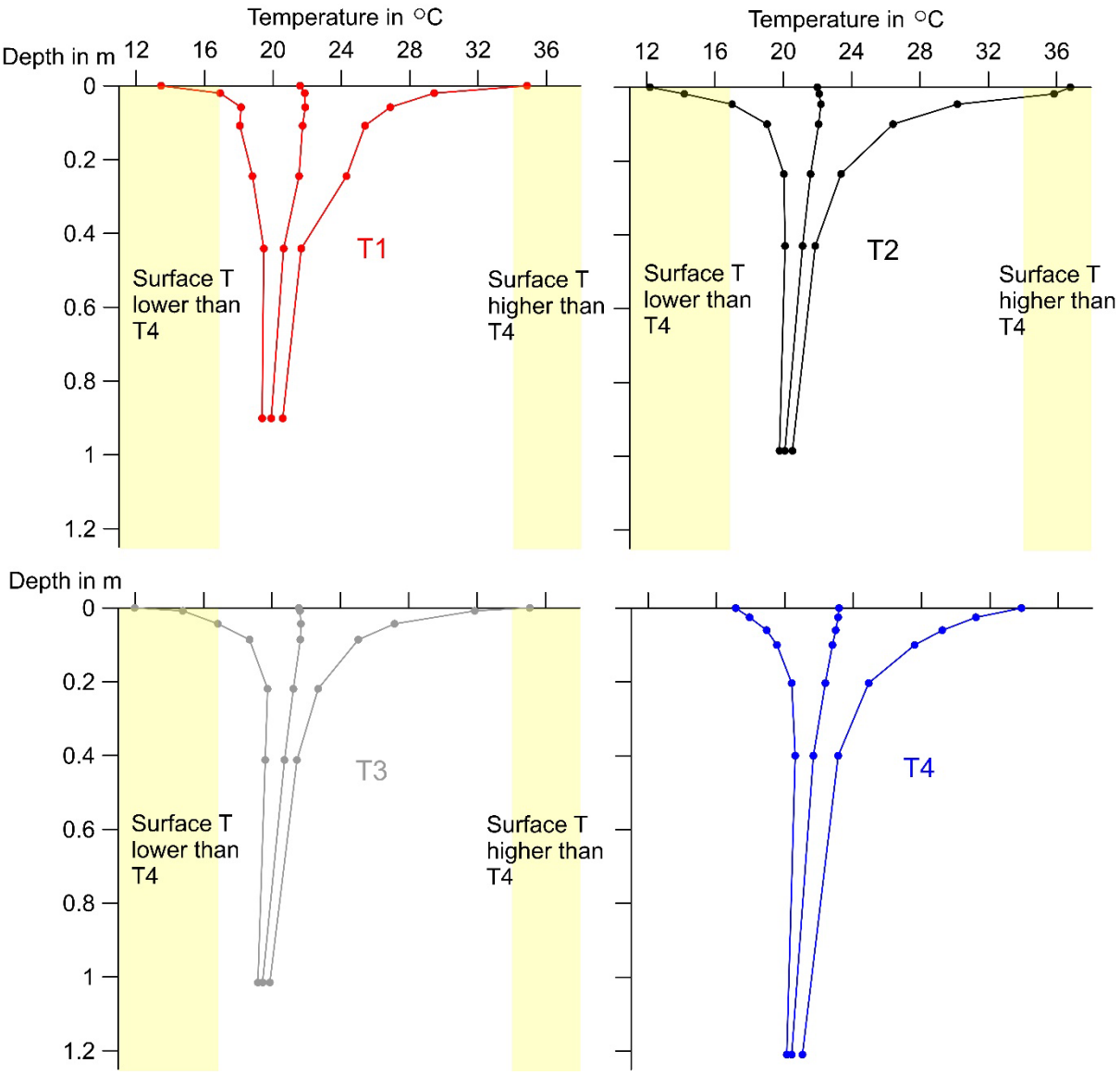

760

761 **Figure 6.** Temperature envelopes of the T-arrays on the mudflats (T1 and T3), the upstream
762 part of the estuarine channel (T2) and the downstream part of the estuarine channel (T4) as
763 dotted line graphs. The dots indicate the measured values of the maximum, minimum and
764 average temperatures measured during sampling. Temperatures within the yellow bars were
765 above or below the values measured at T4. T4, constantly inundated, shows the smallest range
766 of temperature, especially near the surface (see yellow bars). Temperature variations are strong
767 near the surface-sediment interface but decrease quickly with depth. T4 shows the highest
768 average temperatures. The stronger temperature variation of the 0.23 m logger of T1 was likely
769 related to a technical problem, hence it was not used for the heat transport analysis.

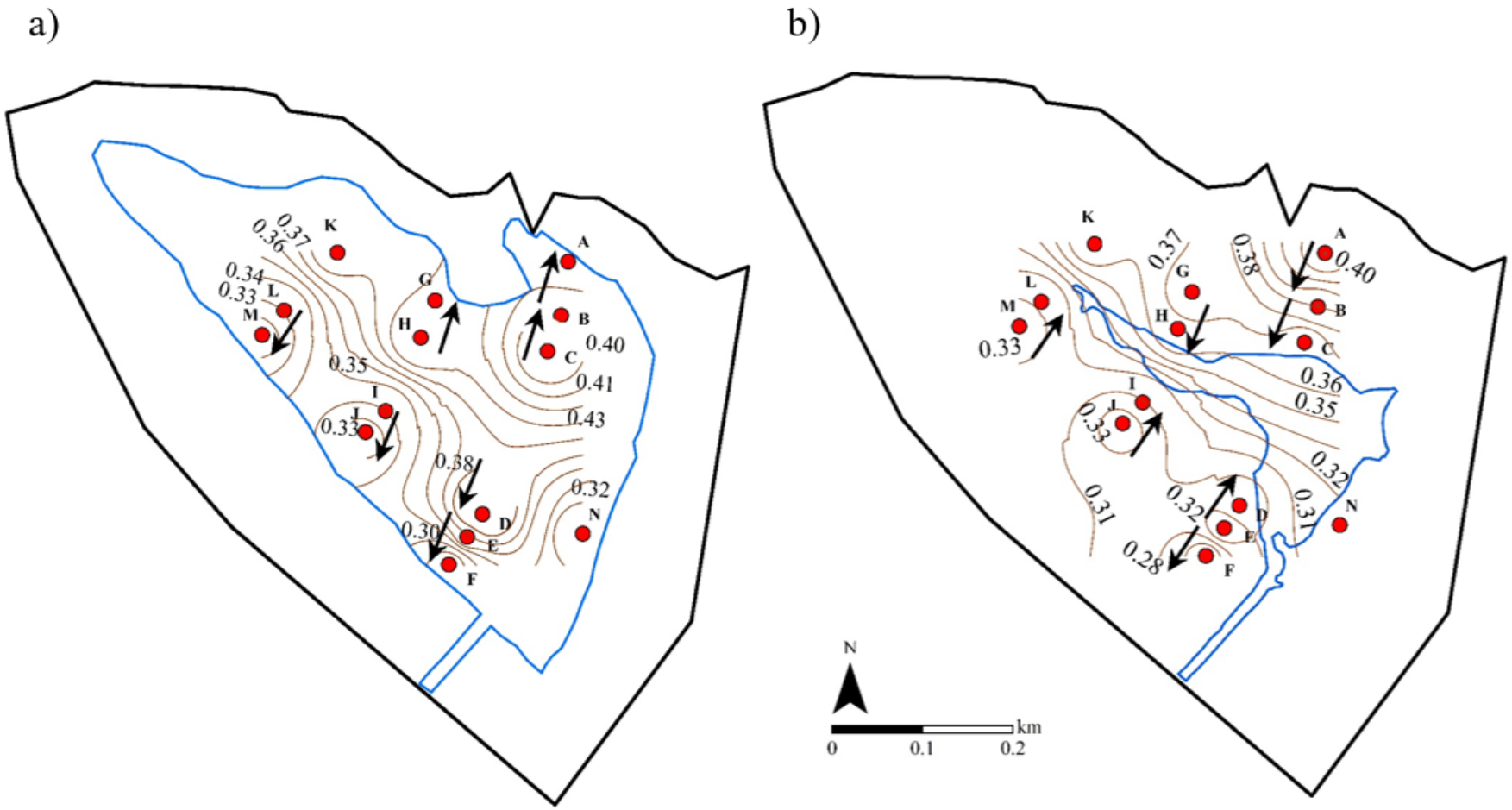

Figure 7. Subsurface flow maps for the study site based on spatial interpolation of measured hydraulic heads for (a) highest and (b) lowest tide during the experiment period. The shown values are interpolated hydraulic heads above an Australian Head Datum (AHD) measured in m. The solid black line indicates catchment boundary while the solid blue line shows the tidal extent at (a) highest and (b) lowest low tide during sampling.

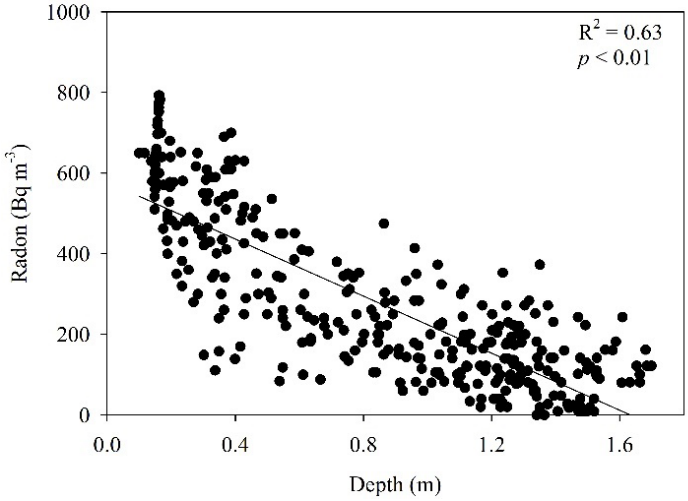

775

776 **Figure 8.** Surface water radon versus depth in the estuary channel indicating tidal pumping as
777 the major driver of subsurface flow at the site.

778

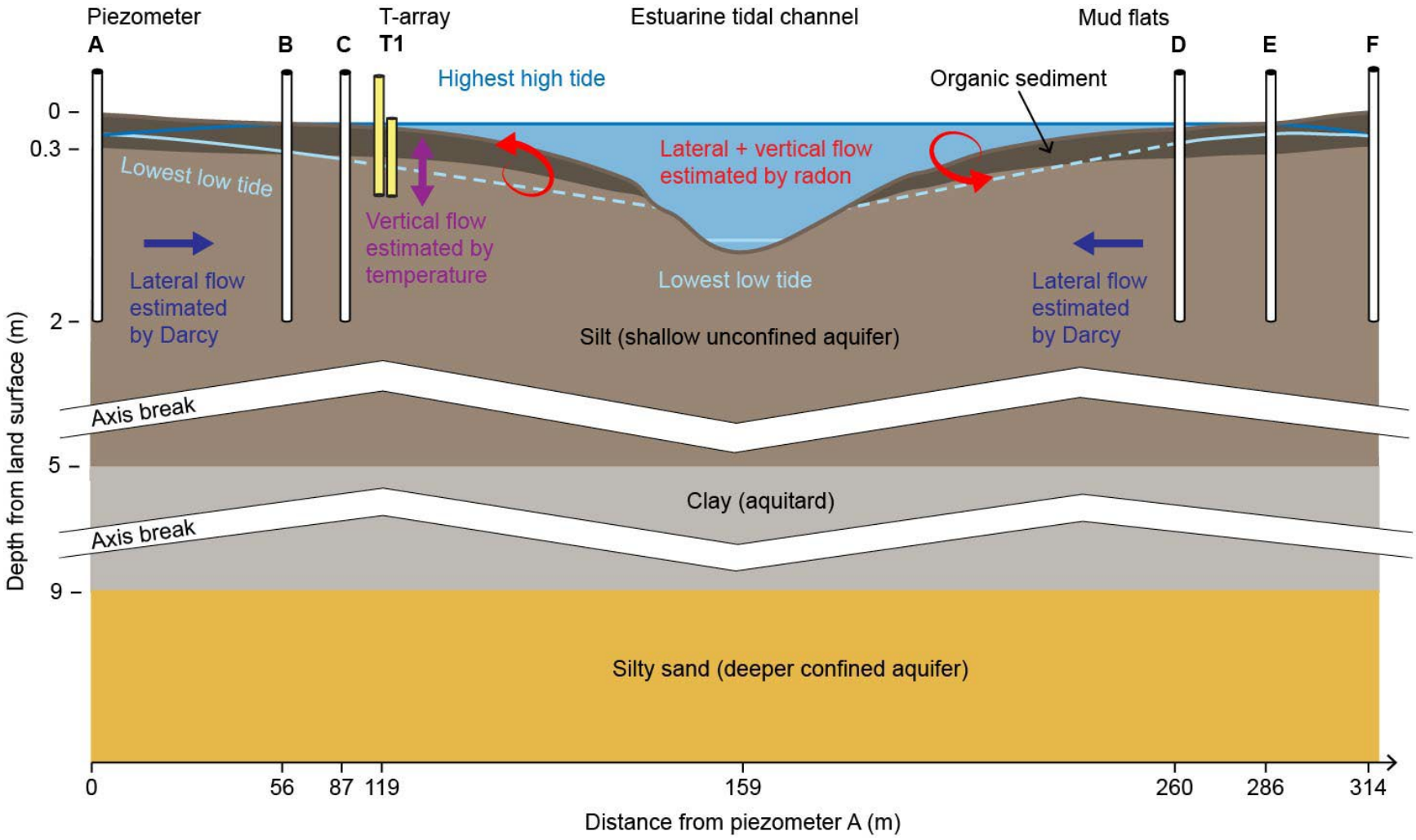

Figure 9. Conceptual figure illustrating the subsurface flow dynamics during highest and lowest tide in the wetland. Head gradients quantify lateral flow, temperature measurements quantify vertical flow and radon quantifies total (lateral + vertical) flow. Solid lines indicate measured surface water level and water table at highest and lowest tide while dash lines indicate assumed location of water table at lowest tide.

7 References

Andersen, M., Baron, L., Gudbjerg, J., Chapellier, D., Jakobsen, R., Gregersen, J., Postma, D., 2007. Nitrate-rich groundwater discharging into a coastal marine environment. Journal of Hydrology 336, 98-114.

Anibas, C., Buis, K., Verhoeven, R., Meire, P., Batelaan, O., 2011. A simple thermal mapping method for seasonal spatial patterns of groundwater–surface water interaction. Journal of Hydrology 397, 93-104.

Anibas, C., Schneidewind, U., Vandersteen, G., Joris, I., Seuntjens, P., Batelaan, O., 2016. From streambed temperature measurements to spatial-temporal flux quantification: using the LPML method to study groundwater–surface water interaction. Hydrological Processes 30, 203-216.

Anibas, C., Verbeiren, B., Buis, K., Chormanski, J., De Doncker, L., Okruszko, T., Meire, P., Batelaan, O., 2012. A hierarchical approach on groundwater-surface water interaction in wetlands along the upper Biebrza River, Poland. Hydrology and Earth System Sciences 16, 2329-2346.

Beck, A.J., Kellum, A.A., Luek, J.L., Cochran, M.A., 2015. Chemical Flux Associated with Spatially and Temporally Variable Submarine Groundwater Discharge, and Chemical Modification in the Subterranean Estuary at Gloucester Point, VA (USA). Estuaries and Coasts, 1-12.

Beebe, D.A., Lowery, B.A., 2018. Seawater recirculation drives groundwater nutrient loading from a developed estuary shoreline with on-site wastewater treatment systems: Mobile Bay, USA. Environmental Earth Sciences 77.

Befus, K.M., Cardenas, M.B., Erler, D.V., Santos, I.R., Eyre, B.D., 2013. Heat transport dynamics at a sandy intertidal zone. Water Resources Research 49, 3770-3786.

Borges, A., Delille, B., Schiettecatte, L.-S., Gazeau, F., Abril, G., Frankignoulle, M., 2004. Gas transfer velocities of CO2 in three European estuaries (Randers Fjord, Scheldt and Thames). Limnology & Oceanography 49.

Bravo, H.R., Jiang, F., Hunt, R.J., 2002. Using groundwater temperature data to constrain parameter estimation in a groundwater flow model of a wetland system. Water Resources Research 38, 28-21-28-14.

Bullock, A., Acreman, M., 2003. The role of wetlands in the hydrological cycle.

Burnett, W., 2008. Radon as a tracer of submarine groundwater discharge. Nuclear and Isotopic Techniques for the Characterization of Submarine Groundwater Discharge in Coastal Zones, 93.

Burnett, W.C., Dulaiova, H., 2003. Estimating the dynamics of groundwater input into the coastal zone via continuous radon-222 measurements. Journal of Environmental Radioactivity 69, 21-35.

Burnett, W.C., Santos, I.R., Weinstein, Y., Swarzenski, P.W., Herut, B., 2007. Remaining uncertainties in the use of Rn-222 as a quantitative tracer of submarine groundwater discharge. IAHS-AISH publication, 109-118.

Burnett, W.C., Taniguchi, M., Oberdorfer, J., 2001. Measurement and significance of the direct discharge of groundwater into the coastal zone. Journal of Sea Research 46, 109-116.

Call, M., Maher, D., Santos, I., Ruiz-Halpern, S., Mangion, P., Sanders, C., Erler, D., Oakes, J., Rosentreter, J., Murray, R., 2015. Spatial and temporal variability of carbon dioxide and methane fluxes over semi-diurnal and spring-neap-spring timescales in a mangrove creek. Geochimica et Cosmochimica Acta.

Cho, H.M., Kim, G., Kwon, E.Y., Moosdorf, N., Garcia-Orellana, J., Santos, I.R., 2018. Radium tracing nutrient inputs through submarine groundwater discharge in the global ocean. Sci Rep 8, 2439.

Conant, B., Robinson, C.E., Hinton, M.J., Russell, H.A.J., 2019. A framework for conceptualizing groundwater-surface water interactions and identifying potential impacts on water quality, water quantity, and ecosystems. Journal of Hydrology 574, 609-627.

Cook, P.G., Rodellas, V., Andrisoa, A., Stieglitz, T.C., 2018a. Exchange across the sediment-water interface quantified from porewater radon profiles. Journal of Hydrology 559, 873-883.

Cook, P.G., Rodellas, V., Stieglitz, T.C., 2018b. Quantifying Surface Water, Porewater and Groundwater Interactions Using Tracers: Tracer Fluxes, Water Fluxes and Endmember Concentrations. Water Resources Research.

Cranswick, R.H., Cook, P.G., Lamontagne, S., 2014. Hyporheic zone exchange fluxes and residence times inferred from riverbed temperature and radon data. Journal of Hydrology 519, 1870-1881.

Darcy, H.P.G., 1856. Les Fontaines publiques de la ville de Dijon. Exposition et application des principes à suivre et des formules à employer dans les questions de distribution d'eau, etc. V. Dalamont.
Davis, K., Santos, I.R., Perkins, A.K., Webb, J.R., Gleeson, J., 2020. Altered groundwater discharge and associated carbon fluxes in a wetland-drained coastal canal. Estuarine, Coastal and Shelf Science 235, 106567.
del Pilar Alvarez, M., Carol, E., Hernández, M.A., Bouza, P.J., 2015. Groundwater dynamic, temperature and salinity response to the tide in Patagonian marshes: Observations on a coastal wetland in San José Gulf, Argentina. Journal of South American Earth Sciences 62, 1-11.
Dimova, N.T., Burnett, W.C., Jeffrey P. Chanton, Corbett, J.E., 2013. Application of radon-222 to investigate groundwater discharge into small shallow lakes. Journal of Hydrology 486, 112–122.
Douglas, A.R., Murgulet, D., Peterson, R.N., 2020. Submarine groundwater discharge in an anthropogenically disturbed, semi-arid estuary. Journal of Hydrology 580, 124369.
Dujardin, J., Anibas, C., Bronders, J., Jamin, P., Hamonts, K., Dejonghe, W., Brouyère, S., Batelaan, O., 2014. Combining flux estimation techniques to improve characterization of groundwater–surface-water interaction in the Zenne River, Belgium. Hydrogeology journal 22, 1657-1668.
Dulaiova, H., Burnett, W., 2006. Radon loss across the water-air interface (Gulf of Thailand) estimated experimentally from 222Rn-224Ra. Geophysical Research Letters 33.
Dulaiova, H., Peterson, R., Burnett, W.C., Lane-Smith, D., 2005. A multi-detector continuous monitor for assessment of ^{222}Rn in the coastal ocean. Journal of Radioanalytical and Nuclear Chemistry 263, 361–365.
Ferguson, G., Bense, V., 2011. Uncertainty in 1D heat-flow analysis to estimate groundwater discharge to a stream. Groundwater 49, 336-347.
Gilfedder, B., Frei, S., Hofmann, H., Cartwright, I., 2015. Groundwater discharge to wetlands driven by storm and flood events: quantification using continuous Radon-222 and electrical conductivity measurements and dynamic mass-balance modelling. Geochimica et Cosmochimica Acta.
Guo, H., Noormets, A., Zhao, B., Chen, J., Sun, G., Gu, Y., Li, B., Chen, J., 2009. Tidal effects on net ecosystem exchange of carbon in an estuarine wetland. Agricultural and Forest Meteorology 149, 1820-1828.
Halloran, L.J., Andersen, M.S., Rau, G.C., 2017. Investigation of the thermal regime and subsurface properties of a tidally affected, variably saturated streambed. Hydrological Processes 31, 2541-2555.
Hays, R.L., Ullman, W.J., 2007. Direct determination of total and fresh groundwater discharge and nutrient loads from a sandy beachface at low tide (Cape Henlopen, Delaware). Limnology and Oceanography 52, 240-247.
Hoehn, E., Cirpka, O., 2006. Assessing hyporheic zone dynamics in two alluvial flood plains of the Southern Alps using water temperature and tracers.
Hunt, R.J., Krabbenhoft, D.P., Anderson, M.P., 1996. Groundwater inflow measurements in wetland systems. Water Resources Research 32, 495-507.
Hwang, D., Lee, Y.-W., Kim, G., 2005. Large submarine groundwater discharge and benthic eutrophication in Bangdu Bay on volcanic Jeju Island, Korea. Limnology and Oceanography 50, 1393-1403.
Johnston, S.G., Keene, A.F., Bush, R.T., Sullivan, L.A., Wong, V.N.L., 2011. Tidally driven water column hydro-geochemistry in a remediating acidic wetland. Journal of Hydrology 409, 128-139.
Jones, S.R., 2013. Geo-environmental challenges of a major coal terminal development in Australia, Proceedings of the 18th International Conference on Soil Mechanics and Geotechnical Engineering, France.
Karan, S., Engesgaard, P., Looms, M.C., Laier, T., Kazmierczak, J., 2013. Groundwater flow and mixing in a wetland–stream system: Field study and numerical modeling. Journal of hydrology 488, 73-83.
Kim, G., Burnett, W., Dulaiova, H., Swarzenski, P., Moore, W., 2001. Measurement of 224Ra and 226Ra activities in natural waters using a radon-in-air monitor. Environmental Science & Technology 35, 4680-4683.
Knights, D., Parks, K.C., Sawyer, A.H., David, C.H., Browning, T.N., Danner, K.M., Wallace, C.D., 2017. Direct groundwater discharge and vulnerability to hidden nutrient loads along the Great Lakes coast of the United States. Journal of hydrology 554, 331-341.

Kurylyk, B.L., Irvine, D.J., Bense, V.F., 2019. Theory, tools, and multidisciplinary applications for tracing groundwater fluxes from temperature profiles. Wiley Interdisciplinary Reviews: Water 6, e1329.
Kurylyk, B.L., Irvine, D.J., Mohammed, A.A., Bense, V.F., Briggs, M.A., Loder, J.W., Geshelin, Y., 2018. Rethinking the use of seabed sediment temperature profiles to trace submarine groundwater flow. Water Resources Research 54, 4595-4614.
Kwon, E.Y., Kim, G., Primeau, F., Moore, W.S., Cho, H.M., DeVries, T., Sarmiento, J.L., Charette, M.A., Cho, Y.K., 2014. Global estimate of submarine groundwater discharge based on an observationally constrained radium isotope model. Geophysical Research Letters 41, 8438-8444.
Lautz, L.K., 2010. Impacts of nonideal field conditions on vertical water velocity estimates from streambed temperature time series. Water Resources Research 46.
Lee, J.-M., Kim, G., 2006. A simple and rapid method for analyzing radon in coastal and ground waters using a radon-in-air monitor. Journal of environmental radioactivity 89, 219-228.
Leote, C., Ibánhez, J.S., Rocha, C., 2008. Submarine groundwater discharge as a nitrogen source to the Ria Formosa studied with seepage meters. Biogeochemistry 88, 185-194.
Li, S., Dong, L., Chen, J., Li, R., Yang, Z., Liang, Z., 2019. Vertical groundwater flux estimation from borehole temperature profiles by a numerical model, RFLUX. Hydrological Processes 33, 1542-1552.
MacIntyre, S., Wanninkhof, R., Chanton, J., 1995. Trace gas exchange across the air-water interface in freshwater and coastal marine environments. Biogenic trace gases: Measuring emissions from soil and water, 52-97.
Makings, U., Santos, I.R., Maher, D.T., Golsby-Smith, L., Eyre, B.D., 2014. Importance of budgets for estimating the input of groundwater-derived nutrients to an eutrophic tidal river and estuary. Estuarine, Coastal and Shelf Science 143, 65-76.
McCallum, A.M., Andersen, M.S., Rau, G.C., Larsen, J.R., Acworth, R.I., 2014. River-aquifer interactions in a semiarid environment investigated using point and reach measurements. Water Resources Research 50, 2815-2829.
McLaughlin, D.L., Cohen, M.J., 2013. Realizing ecosystem services: wetland hydrologic function along a gradient of ecosystem condition. Ecological Applications 23, 1619-1631.
Montiel, D., Dimova, N., Andreo, B., Prieto, J., García-Orellana, J., Rodellas, V., 2018. Assessing submarine groundwater discharge (SGD) and nitrate fluxes in highly heterogeneous coastal karst aquifers: Challenges and solutions. Journal of Hydrology 557, 222-242.
Moore, W.S., 2003. Sources and fluxes of submarine groundwater discharge delineated by radium isotopes. Biogeochemistry 75–93, 75–93.
Moore, W.S., 2006. The role of submarine groundwater discharge in coastal biogeochemistry. Journal of Geochemical Exploration 88, 389-393.
Moore, W.S., 2010. The effect of submarine groundwater discharge on the ocean. The Annual Review of Marine Science 2, 59-88.
Mulligan, A.E., Charette, M.A., 2006. Intercomparison of submarine groundwater discharge estimates from a sandy unconfined aquifer. Journal of Hydrology 327, 411-425.
Muneepeerakul, C.P., Miralles-Wilhelm, F., Tamea, S., Rinaldo, A., Rodriguez-Iturbe, I., 2008. Coupled hydrologic and vegetation dynamics in wetland ecosystems. Water Resources Research 44.
Navarro-Martinez, F., Garcia, A.S., Sánchez-Martos, F., Espasa, A.B., Sánchez, L.M., Perulero, A.R., 2017. Radionuclides as natural tracers of the interaction between groundwater and surface water in the River Andarax, Spain. Journal of environmental radioactivity 180, 9-18.
Noori, S., Ebrahimi, K., Liaghat, A.-M., Hoorfar, A.-H., 2013. Comparison of different geostatistical methods to estimate groundwater level at different climatic periods. Water and Environment Journal 27, 10-19.
Peterson, R.N., Burnett, W.C., Taniguchi, M., Chen, J., Santos, I.R., Ishitobi, T., 2008. Radon and radium isotope assessment of submarine groundwater discharge in the Yellow River delta, China. JOURNAL OF GEOPHYSICAL RESEARCH 113, 9 - 21.
Peterson, R.N., Meile, C., Peterson, L.E., Carter, M., Miklesh, D., 2019. Groundwater discharge dynamics into a salt marsh tidal river. Estuarine, Coastal and Shelf Science 218, 324-333.
Porubsky, W.P., Weston, N.B., Mooreb, W.S., Ruppel, C., Joye, S.B., 2014. Dynamics of submarine groundwater discharge and associated fluxes of dissolved nutrients, carbon, and trace gases to the

coastal zone (Okatee River estuary, South Carolina). Geochimica et Cosmochimica Acta 131 81–97.
Qu, W.J., Li, H.L., Huang, H., Zheng, C.M., Wang, C.Y., Wang, X.J., Zhang, Y., 2017. Seawater-groundwater exchange and nutrients carried by submarine groundwater discharge in different types of wetlands at Jiaozhou Bay, China. Journal of Hydrology 555, 185-197.
Rakhimbekova, S., O'Carroll, D.M., Andersen, M.S., Wu, M.Z., Robinson, C.E., 2018. Effect of transient wave forcing on the behavior of arsenic in a nearshore aquifer. Environmental science & technology 52, 12338-12348.
Rau, G.C., Andersen, M.S., McCallum, A.M., Acworth, R.I., 2010. Analytical methods that use natural heat as a tracer to quantify surface water–groundwater exchange, evaluated using field temperature records. Hydrogeology journal 18, 1093-1110.
Rau, G.C., Andersen, M.S., McCallum, A.M., Roshan, H., Acworth, R.I., 2014. Heat as a tracer to quantify water flow in near-surface sediments. Earth-Science Reviews 129, 40-58.
Rau, G.C., Cuthbert, M.O., McCallum, A.M., Halloran, L.J., Andersen, M.S., 2015. Assessing the accuracy of 1-D analytical heat tracing for estimating near-surface sediment thermal diffusivity and water flux under transient conditions. Journal of Geophysical Research: Earth Surface 120, 1551-1573.
Ren, J., Cheng, J., Yang, J., Zhou, Y., 2018. A review on using heat as a tool for studying groundwater–surface water interactions. Environmental earth sciences 77, 756.
Robinson, F., 2006. Land Contamination and Groundwater Assessment (Kooragang Island). RCA Australia, Australia.
Rodellas, V., Garcia-Orellana, J., Masqué, P., Feldman, M., Weinstein, Y., 2015. Submarine groundwater discharge as a major source of nutrients to the Mediterranean Sea. Proceedings of the National Academy of Sciences 112, 3926-3930.
Rosenberry, D.O., Duque, C., Lee, D.R., 2020. History and evolution of seepage meters for quantifying flow between groundwater and surface water: Part 1–Freshwater settings. Earth-Science Reviews, 103167.
Roshan, H., Rau, G.C., Andersen, M.S., Acworth, I.R., 2012. Use of heat as tracer to quantify vertical streambed flow in a two-dimensional flow field. Water Resources Research 48.
Sadat-Noori, M., Glamore, W., 2019. Porewater exchange drives trace metal, dissolved organic carbon and total dissolved nitrogen export from a temperate mangrove wetland. Journal of environmental management 248, 109264.
Sadat-Noori, M., Santos, I.R., Sanders, C.J., Sanders, L.M., Maher, D.T., 2015. Groundwater Discharge into an Estuary Using Spatially Distributed Radon Time Series and Radium Isotopes. Journal of Hydrology.
Sadat-Noori, M., Santos, I.R., Tait, D.R., Maher, D.T., 2016a. Fresh meteoric versus recirculated saline groundwater nutrient inputs into a subtropical estuary. The Science of the total environment 566-567, 1440-1453.
Sadat-Noori, M., Santos, I.R., Tait, D.R., McMahon, A., Kadel, S., Maher, D.T., 2016b. Intermittently Closed and Open Lakes and/or Lagoons (ICOLLs) as groundwater-dominated coastal systems: Evidence from seasonal radon observations. Journal of Hydrology 535, 612-624.
Sadat-Noori, M., Tait, D.R., Maher, D.T., Holloway, C., Santos, I.R., 2017. Greenhouse gases and submarine groundwater discharge in a Sydney Harbour embayment (Australia). Estuarine, Coastal and Shelf Science.
Santos, I.R., Eyre, B.D., 2011. Radon tracing of groundwater discharge into an Australian estuary surrounded by coastal acid sulphate soils. Journal of hydrology 396, 246-257.
Santos, I.R., Eyre, B.D., Huettel, M., 2012. The driving forces of porewater and groundwater flow in permeable coastal sediments: A review. Estuarine, Coastal and Shelf Science 98, 1- 15.
Santos, I.R., Maher, D.T., Larkin, R., Webb, J.R., Sanders, C.J., 2019. Carbon outwelling and outgassing vs. burial in an estuarine tidal creek surrounded by mangrove and saltmarsh wetlands. Limnology and Oceanography 64, 996-1013.
Schubert, M., Paschke, A., Lieberman, E., Burnett, W.C., 2012. Air–water partitioning of 222Rn and its dependence on water temperature and salinity. Environmental science & technology 46, 3905-3911.

Sebok, E., Müller, S., 2019. The effect of sediment thermal conductivity on vertical groundwater flux estimates. Hydrology & Earth System Sciences 23.
Stieglitz, T.C., Clark, J.F., Hancock, G.J., 2013. The mangrove pump: The tidal flushing of animal burrows in a tropical mangrove forest determined from radionuclide budgets. Geochimica et Cosmochimica Acta 102, 12-22.
Su, N., Burnett, W.C., MacIntyre, H.L., Liefer, J.D., Peterson, R.N., Viso, R., 2014. Natural Radon and Radium Isotopes for Assessing Groundwater Discharge into Little Lagoon, AL: Implications for Harmful Algal Blooms. Estuaries and Coasts 37, 893–910.
Su, X., Cui, G., Du, S., Yuan, W., Wang, H., 2016. Using multiple environmental methods to estimate groundwater discharge into an arid lake (Dakebo Lake, Inner Mongolia, China). Hydrogeology Journal 24, 1707-1722.
Susilo, A., Ridd, P.V., 2005. The bulk hydraulic conductivity of mangrove soil perforated with animal burrows. Wetlands Ecology and Management 13, 123-133.
Swain, E.D., Prinos, S.T., 2018. Using heat as a tracer to determine groundwater seepage in the Indian River Lagoon, Florida, April–November, 2017. US Geological Survey.
Taniguchi, M., Burnett, W.C., Smith, C.F., Paulsen, R.J., O'Rourke, D., Krupa, S.L., Christoff, J.L., 2003. Spatial and temporal distributions of submarine groundwater discharge rates obtained from various types of seepage meters at a site in the Northeastern Gulf of Mexico. Biogeochemistry 66, 35-53.
Turner, I.L., Rau, G.C., Austin, M.J., Andersen, M.S., 2016. Groundwater fluxes and flow paths within coastal barriers: Observations from a large-scale laboratory experiment (BARDEX II). Coastal Engineering 113, 104-116.
Unland, N., Cartwright, I., Andersen, M., Rau, G., Reed, J., Gilfedder, B., Atkinson, A., Hofmann, H., 2013. Investigating the spatio-temporal variability in groundwater and surface water interactions: a multi-technical approach. Hydrology & Earth System Sciences Discussions 10.
Vandersteen, G., Schneidewind, U., Anibas, C., Schmidt, C., Seuntjens, P., Batelaan, O., 2015. Determining groundwater-surface water exchange from temperature-time series: Combining a local polynomial method with a maximum likelihood estimator. Water Resources Research 51, 922-939.
Vogt, T., Hoehn, E., Schneider, P., Freund, A., Schirmer, M., Cirpka, O.A., 2010. Fluctuations of electrical conductivity as a natural tracer for bank filtration in a losing stream. Advances in Water Resources 33, 1296-1308.
Webb, J.R., Santos, I.R., Maher, D.T., Tait, D.R., Cyronak, T., Sadat-Noori, M., Macklin, P., Jeffrey, L.C., 2019. Groundwater as a source of dissolved organic matter to coastal waters: Insights from radon and CDOM observations in 12 shallow coastal systems. Limnology and Oceanography 64, 182-196.
Webb, J.R., Santos, I.R., Robson, B., Macdonald, B., Jeffrey, L., Maher, D.T., 2017. Constraining the annual groundwater contribution to the water balance of an agricultural floodplain using radon: The importance of floods. Water Resources Research 53, 544-562.
Weinstein, Y., Yechieli, Y., Shalem, Y., Burnett, W.C., Swarzenski, P.W., Herut, B., 2011. What is the role of fresh groundwater and recirculated seawater in conveying nutrients to the coastal ocean? Environmental science & technology 45, 5195-5200.
Zlotnik, V., Tartakovsky, D.M., 2018. Interpretation of Heat-Pulse Tracer Tests for Characterization of Three-Dimensional Velocity Fields in Hyporheic Zone. Water Resources Research 54, 4028-4039.